Royal Netherlands
Meteorological Institute
*Ministry of Infrastructure and the Environment*

Utrecht University

# Characterizing the seismic signal of individual wind turbines in the Borgsweer area

**Master thesis**

**B.C.M. van der Vleut**

Student number: 4066073
Supervisors: E.N. Ruigrok and Dr. J.A.M. Paulssen
Faculty of Geosciences, Utrecht University
Utrecht, The Netherlands
March 10, 2019

# Abstract

Wind turbines (WTs) emit seismic signals due to the rotation of the blades and the movement of the tower. These signals can be characterized based on frequency, attenuation, the influence of wind speed and type of seismic waves. The objective of this research is to characterize the seismic signals of individual WTs in the Borgsweer area, Groningen, the Netherlands. This is of great important, since the seismic WT signal can interfere with the monitoring of induced earthquakes in the area. It is important to characterize the seismic signal of WTs since it can be used in the future to study the inversion of subterranean parameters and to update velocity and attenuation models. WT signals are a good source for seismic interferometry due to the continuous signal and stable distribution. A spectral analysis is conducted to untangle the individual signal from the signal of multiple WTs in two steps: I) finding the local combined WT signal by producing power-spectrum densities (PSDs), and II) using a cross-correlation beamforming algorithm to localize the individual WTs. The input to this research is 33 days of recorded noise by the NAM Borgsweer flexible three-component array. The small spacing of the stations provides the opportunity to better characterize individual signals of WTs in contrast to other studies that only were able to detect WT parks due to the large spacing between their stations. A dispersion curve was constructed to estimate the travel times of the seismic waves needed for beamforming. Unfortunately the shallow subsurface was too heterogeneous for the dispersion curve to continue at frequencies higher than 1 Hz. The heterogeneous subsurface leads to an incomplete beamforming localization of the WTs in the area, since the algorithm assumes a homogeneous subsurface. The radiation pattern and the type of seismic wave are characterized as a function of wind direction. Using the PSDs, the influence of wind speed on the signal is determined. Eigenmode frequencies due to the movement of the tower are found for the Delfzijl North (0.63 Hz) and South (0.31 Hz) wind park. Multiples of these frequencies follow the physics of standing waves on a clamped beam. A prominent peak near 2.1 Hz is likely related to the 3P blade rotation.


Cover photo: Natuur en milieu federatie Groningen: https://nmfgroningen.nl/wat-we-doen/klimaat-energie/windenergie/

# Contents


**1 Introduction** **3**
- 1.1 Research objective . . . 3
- 1.2 Previous studies . . . 3
  - 1.2.1 Wind turbine characteristics . . . 3
  - 1.2.2 Types of oscillations . . . 4
  - 1.2.3 Attenuation . . . 5
  - 1.2.4 Type of emitted waves . . . 7
  - 1.2.5 Signal of an individual WT . . . 8
- 1.3 Setting . . . 8

**2 Method** **13**
- 2.1 Power Spectrum Densities . . . 13
- 2.2 Beamforming . . . 14
  - 2.2.1 Conventional beamforming . . . 14
  - 2.2.2 Cross-correlation beamforming . . . 16
- 2.3 Dispersion curves . . . 18
- 2.4 Synthetic test . . . 19
  - 2.4.1 The effect of the position and number of sources within the array on mapping of the sources . . . 20
  - 2.4.2 The effect of applying a cross-coherence or cross-correlation to the data . . . 20
  - 2.4.3 The effect of cross-cohering the data before or after taking the Fourier transform 20
  - 2.4.4 The effect of the frequency of the emitted wave . . . 20
  - 2.4.5 The effect of the velocity of wave propagation . . . 24
  - 2.4.6 The effect of a velocity error between the real velocity $v_{real}$ and the modelled velocity $v_{mod}$ . . . 24

**3 Results** **26**
- 3.1 Local combined WT signal . . . 26
  - 3.1.1 Recording compatibility . . . 26
  - 3.1.2 PSD with varying distance to the WTs . . . 26
  - 3.1.3 PSDs with varying wind speed . . . 27
  - 3.1.4 Spatial PSDs . . . 27
  - 3.1.5 PSDs with varying wind direction . . . 30
- 3.2 Individual WT signal . . . 36
  - 3.2.1 Dispersion curve . . . 36
  - 3.2.2 Beamforming . . . 36

**4 Discussion** **39**
- 4.1 Local combined WT signal . . . 39
  - 4.1.1 Spectral characteristics . . . 39
  - 4.1.2 Radiation pattern . . . 40
- 4.2 Individual WT signal . . . 41
  - 4.2.1 Dispersion curves . . . 41
  - 4.2.2 Beamforming . . . 41
- 4.3 Future studies . . . 41

**5 Conclusion** **42**

**6 Acknowledgements** **42**

**7 References** **43**

**8 Appendix** **46**

# 1 Introduction

## 1.1 Research objective

The largest gas field of Europe with a surface area of 900 $km^2$ is located in the province Groningen, the Netherlands. The NAM (Nederlandse Aardolie Maatschappij) operates this gas field since 1963. The exploration of the gas field has led to induced seismicity, with the first recorded earthquake in 1991. This induced seismicity called for the installation of a new geophone and accelerometer network that covers the area of the seismicity well: the G-network was in operation by 2015 (Dost et al., 2017). This dense seismic network provides opportunities to study influences of additional seismic sources to the induced seismicity. Among these are seismic signals produced by wind turbines (WTs). Two large WT parks are placed in Groningen: Eemshaven and Delfzijl (Figure 5). The research on WT signals is an important addition to monitoring the induced seisimicity, since a WT signal might overpower the induced seismic signals in surveys by acting as a constant infrasound and seismic source in the same frequency spectrum as the induced seismicity. Furthermore, characterizing the seismic signal of WTs may enable us to update velocity and attenuation models for the Groningen area. Potentially, near surface properties can be monitored using the WT signal for interferometry. Jagt (2017) used the G-network to study seismic signals induced by the different WTs in Delfzijl and Eemshaven and obtained characteristics of the different WT parks. However, the element spacing in the G-network was too sparse to characterize individual WTs. The NAM has now acquired additional seismic data with the NAM Borgsweer flexnet survey, which encloses partly the Delfzijl WT park. They recorded one month of seismic noise with the objective to better characterize the seismic velocities in the unconsolidated sediments. This dataset, the NAM flexible array, has potential to study the WT seismic signal in more detail due to its well azimuthal coverage of the different WTs. The main goal of this research will be to characterize the seismic signal of a single WT: its spectral characteristics, attenuation, the waves that are induced, and how they vary with wind speed. WTs are a growing business due to their cost-effective sustainable energy. The amount of WTs will grow further due to cost reductions and emission regulations. The dynamics of WT signal propagation are not fully understood and the seismic signals of single WTs in Groningen have never completely been characterized. The main goal of this study is the characterization of an individual WT signal to enable further research of the influence of the signals on nearby seismic stations and subsurface properties.

## 1.2 Previous studies

The problem of WT signals interfering with seismic stations has led to several studies after the seismic signals of WTs. These studies included research after wind turbine characteristics, types of oscillations, attenuation of the signal, type of emitted waves, and influence of wind speed.

### 1.2.1 Wind turbine characteristics

WT systems consist of five components: the rotor, transmission, generator, control system, and support structure (Van der Tempel and Molenaar, 2002). Figure 1 gives an schematic overview of the components. The rotor is a combination of the blades and the hub and rotates under the influence of wind hitting the blades. The wind lifts and rotates the blades. The pitch system is located in the rotor and has the ability to control rotation speed by turning the blades away from the wind (Eneco, 2017). The transmission system transmits the rotation to the generator, which produces electricity within the turbine. The control system can start and stop the turbine when the conditions change and has control over the gear box. The conditions are measured by the anemometer and the wind vane that are located on top of the nacelle. The structure is supported by the tower, which is linked to the turbine with a yaw drive. In case of changing wind direction, the yaw drive orients the nacelle in the most favourable position. The tower is built on a concrete foundation in the case of the onshore wind turbines of this study.

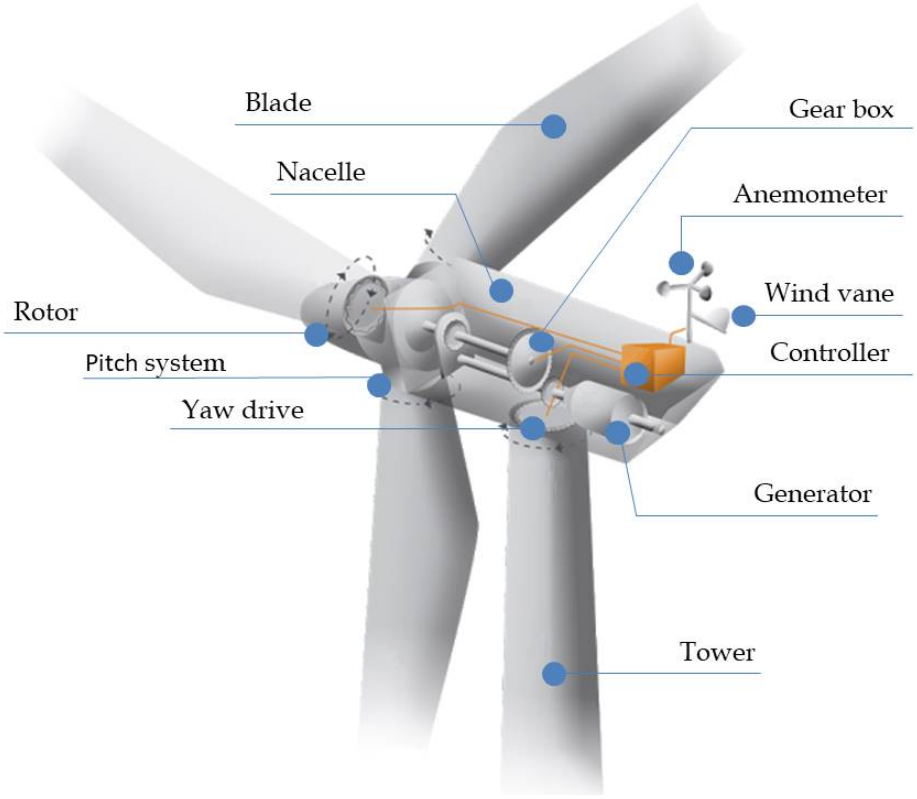


Figure 1: Components of a wind turbine. Modified after DotX Control Solutions B.V. (2018)

### 1.2.2 Types of oscillations

WTs are a continuous source of seismic waves. The tower oscillates due to the influence of wind and transfers these oscillations to the subsurface through the strong coupling of the large concrete foundation (Saccorotti et al., 2011). The Delfzijl WT park is an onshore facility and therefore the influence of waves and damping of water that an offshore WT park would experience will not be discussed. Van der Tempel and Molenaar (2002) have studied the oscillations of WTs. They found two distinct types of oscillations: oscillations due to the rotation of the blades and oscillations depending on the eigenmodes and higher harmonics of the WT's complete construction. Oscillations due to rotation of the blades have two distinct frequencies: blade-passing frequencies and rotation frequencies. Both are due to excitation of the rotor blades by the wind. Blade-passing frequencies, 3P for a WT with three blades and 2P for a WT with two blades, are due to the blades passing a reference point on the rotation circle. Rotation frequencies (1P) are due to the full rotation of a single blade. The 3P frequency is therefore three times the frequency of the 1P (Van der Tempel and Molenaar, 2002). These frequencies are not allowed to excite one another, because this would lead to resonance that can destruct the WT. Most seismic studies concentrate on blade-passing frequencies and their harmonics, since these are most easy detectable. Schofield (2001), Styles et al. (2005), and Zieger and Ritter (2018) found harmonics of fundamental blade-passing frequencies which were respectively 1.47 Hz, 0.5 Hz, and 0.92 Hz. Saccorotti et al. (2011) found that the spectrum changes when the wave propagates away from the WT. The unexplained peaks in the seismic amplitude spectrum could be due to interference with other WT waves and resonance of the subsurface (Stammler and Ceranna, 2016).

Stiffness of foundation influences the eigenfrequencies and therefore these may vary. Saccorotti et al. (2011) found amplitude peaks which originated from WTs while the blades were not rotating. They concluded that these must be due to the eigenmodes of the WTs construction as a whole. As a logical

result, these eigenmode oscillations do not increase in frequency with increased wind speed, but only in amplitude. Rotational and blade-passing oscillations do increase in frequency when wind speed increases, since the blades will rotate faster (e.g. Saccorotti et al. (2011), Westwood et al. (2015), Stammler and Ceranna (2016), Jagt (2017), Neuffer and Kremers (2017), and Friedrich et al. (2018)). Note that the use of the gearbox minimizes this frequency increase. Eigenfrequencies are hard to measure, since they are in the spectrum of microseism of e.g. the ocean (Zieger and Ritter, 2018). Devriendt et al. (2014) did a study after the eigenfrequencies of offshore Vestas V90-3MW turbines and found a frequency of 0.361 Hz in the thrust-wise direction and 0.366 Hz in the sideway direction. per turbine. Devriendt et al. (2014) imaged the eigenmode shapes of WTs (Figure 2). The tower can move in two directions. One eigenmode is the for-aft (FA) mode. Another eigenmode is the side-side (SS) bending mode. During these modes the nacelle experiences a displacement that is dependent on the mode. A WT follows most likely the physics for a standing wave on a clamped beam (Figure 3). This means that the frequency of a mode ($f_m$) can be found from the fundamental frequency ($f_0$) and the number of the mode ($m$) using:

$$f_m = (2m - 1)f_0 \tag{1}$$

The eigenfrequencies do not influence the blade-passing frequencies (Xi Engineering Consultants Ltd, 2014). Jagt (2017) found possible fundmental eigenfrequencies of 0.39 Hz at the Delfzijl South wind park and 0.63 Hz for the Delfzijl North wind park. Neuffer and Kremers (2017) concluded that the hub height is the defining parameter controlling the frequencies of the radiated seismic waves due to eigenmodes of the WT. Van der Tempel and Molenaar (2002) established a formula for the fundamental eigenfrequency:

$$f_0 \cong \frac{D}{L^2}\sqrt{\frac{E}{104(a + 0.227)\rho_c}} \tag{2}$$

Here $f_0$ is the fundamental eigenfrequency, $D$ is the tower average diameter, $L$ is the tower height, $E$ is the Young's modulus, and $\rho_c$ is the density of the steel. $a$ is given by $\frac{M}{\rho_c \pi DtL}$ in which $M$ is the top mass and $t$ is the tower wall thickness. This equation does not consider flexibility of the foundation and the stiffness softening effect due to the axial load (mass of the rotor and blade system) (Adhikari and Bhattacharya, 2012). Therefore Adhikari and Bhattacharya (2012) established a formula that includes these parameters, but is much more complicated and needs to be calculated numerically. The methods of Adhikari and Bhattacharya (2012) and Van der Tempel and Molenaar (2002) seem a good estimate, but are hard to calculate for WTs of which the specifics like the Young's modulus are unknown. The estimations of Devriendt et al. (2014) and Jagt (2017) are a good approximation for the expected fundamental eigenfrequency of the WTs in this study. The sequence of overtones should be determined by Equation 1.

### 1.2.3 Attenuation

The distance over which the receivers can still measure the seismic waves emitted by the WTs over the background noise varies largely and is due to relative amplitude and attenuation of the waves. These factors are influenced by the type of WT, wind speed and direction, the frequency, damping, topography and subsurface properties. It is important to know the decay distance in order to asses possible influence on seismic stations. Stammler and Ceranna (2016) found that higher frequencies decay faster away from the WT than lower frequencies, which is in agreement with the theory of Sato et al. (2012). They did not include frequencies higher than 7 Hz in the spectrum. Others took a top frequency of 10 Hz (e.g. Zieger and Ritter (2018); Neuffer and Kremers (2017)). The largest distance were the signal of the WT was still distinguishable in a study was 18 km, found by Schofield (2001) in Oregon. Stammler and Ceranna (2016) found a distance of 15 km, which was also found by numerical modeling (Gortsas et al., 2017). Saccorotti et al. (2011) found 11 km distance, Zieger and Ritter (2018) found 5.5 km, and Estrella et al. (2017) found 9 and 4 km for two different wind farms. Jagt (2017) could still detect the WT-related frequency 2.1 Hz at 6.2 km from Delfzijl North and 4 km from Delfzijl

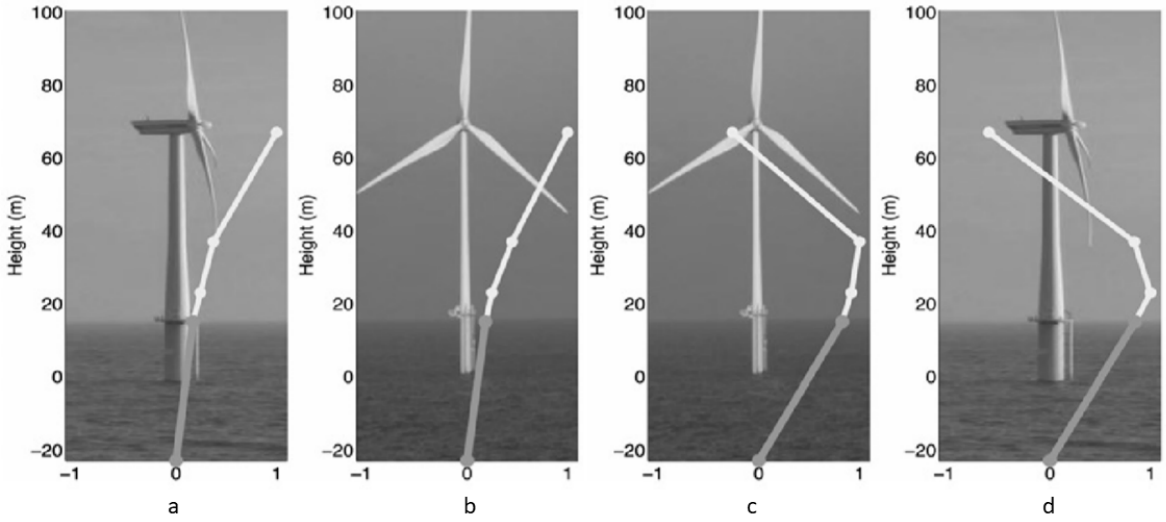


Figure 2: Four identified dominant mode shapes. From left to right: a) First FA bending mode, FA1, b) First SS bending mode, SS1, c)Mode with a second SS bending mode tower and nacelle component, SS2N, e) Mode with a second FA bending mode tower and nacelle component, FA2N (Devriendt et al., 2014).

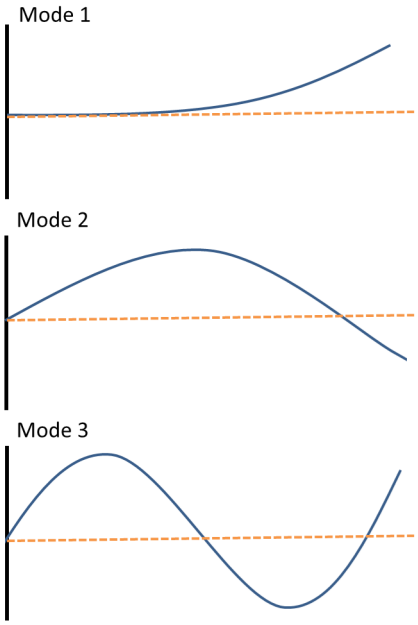


Figure 3: Schematic overview of the first three modes of a standing wave on a clamped beam.

South. The array of this study is well within those boundaries.

Studies tried to fit a formula to the distance over which a WT signal can still be recorded ($R$) to be able to describe the attenuation. Schofield (2001) found that the attenuation is equal to $1/R$, but Estrella et al. (2017) found more variations and therefore stated that the attenuation is described by $C/R^b$ with a $b$ value between 0.73 and 1.87 for a frequency of 2.7-4.5 Hz. These values correspond with 0.77-1.59 found by Zieger and Ritter (2018) for far-field, though they could not fit all data samples for

frequencies lower than 5 Hz. Stammler and Ceranna (2016) found a higher value: $b$=2.7, which is in accordance with Neuffer and Kremers (2017): $b$=2.42-2.78. The value for $b$ increases with increasing frequency. This might be due to scattering and anelastic attenuation effects along the path of the wave (Sato et al., 2012). Zieger and Ritter (2018) found that the amplitude decreases with distance as well as with depth from the WT. The wind dependent signals decrease fastest with depth. This information is useful for making choices in source-receiver distances in the beamforming of our study.

### 1.2.4 Type of emitted waves

Many studies find that WTs emit surface waves. Westwood and Styles (2017) found evidence of both Love and Rayleigh waves for blade rotation frequencies, based on the propagation velocity of the waves. Xi Engineering Consultants Ltd (2014), Styles et al. (2005), Neuffer and Kremers (2017), and Friedrich et al. (2018) assume the propagating waves to be Rayleigh waves. This is supported by Gortsas et al. (2017), who numerically found the Rayleigh wave propagation. Saccorotti et al. (2011) concluded that the WTs might also emit body waves in addition to Love waves, consisting of P, SV and SH waves. It is hard to make a general assumption, since the emitted waves are largely dependent on the geology of the subsurface. The presence of surface waves is though illustrated by the decaying amplitude of the signals with depth (Zieger and Ritter, 2018). Schofield (2001) and Saccorotti et al. (2011) found that it might also be possible that infrasound is produced by the WT that later continues in the subsurface as seismic waves. Friedrich et al. (2018) contradicts that and concludes that the typical group velocities of about 320 m/s are due to Rayleigh waves radiated by eigenmodes of the WT tower.

With the knowledge that all WTs in the study area have yaw control, it can be stated that, unless the wind speed is extreme, the wind will always push the tower of the WT to a FA motion, since the blades will be oriented perpendicular to the wind direction. Rotation of the blades might add a slight

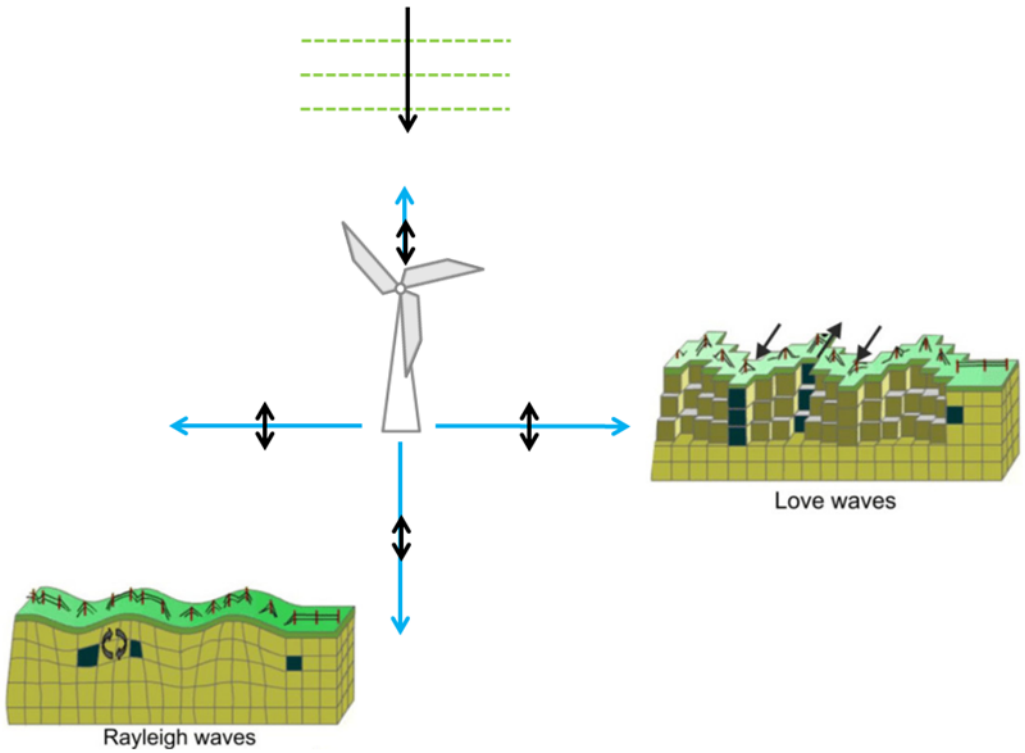


Figure 4: Schematic overview of the seismic radiation pattern of a WT. The Love and Rayleigh wave drawings have been modified from Grotzinger et al. (2010).

SS component, but we assume this to be minor. With these assumptions a seismic radiation pattern of surface waves like in Figure 4 is hypothesized.

Changes in radiation from the WTs can be found as a function of different wind directions. Jagt (2017) found that the wind direction did influence the maximum values of the PSD and therefore concluded that the propagating wave is non-radial. Zieger and Ritter (2018) on the other hand found no difference in PSD after comparing two profiles with different azimuth, though neither of the two profiles lie in the wind direction. They see no evidence of changing radiation with wind direction, but suggest further research on the radiation and the effect of wind direction on attenuation. It is useful to describe the radiation pattern of WTs, as it might be varying strongly with wind direction. This could affect results of research after subsurface properties.

### 1.2.5 Signal of an individual WT

The distinction of individual WT signals is a main challenge for seismologists (Zieger and Ritter, 2018). Stammler and Ceranna (2016) tried to achieve it by dividing the PSD by the number of contributing WTs. Zieger and Ritter (2018) speculate that beyond 30 metres of distance to a WT park, the frequency spectrum of the signal is comparable to that of a single WT. Both studies did not find an exact way to obtain and characterize the signal of an individual WT without broad assumptions. This will be the objective of my research.

## 1.3 Setting

The Borgsweer area is located in the west of the province of Groningen, the Netherlands. The province has experienced many induced earthquakes of magnitude $\leq 3.6$ due to gas exploration of the large Groningen gas field. The induced seismicity called for the installation of a new geophone and accelerometer network that covers the area of the seismicity well: the G-network was in operation by 2015. This network was not sufficient for site amplification studies and therefore NAM executed the Borgsweer flexnet survey. A dense network of 415 multichannel stations was placed on multiple locations above the gas field. One of these locations is the Borgsweer area. The array takes up about 48 $km^2$. The flexnet array has been recording from December 21, 2016 until January 23, 2017. The spacing between the instruments is approximately 250-600 m. The array is build up out of 16 rows and 26 columns. Station names are given as 'row.column'. In order to keep the calculations as time-effective as possible, the network is divided into six calculation patches (Figure 7).

Groningen is a province with many WTs due to its flat topography and wind-favourable location. The province contains two wind parks: Eemshaven and Delfzijl (Figure 5). The Delfzijl wind park is divided in the Delfzijl North and the Delfzijl South wind park. Delfzijl North wind park is relatively new (2015) and consists of 19 Nordex N100-3.3MW WTs. Delfzijl South wind park consists of 34 Enercon E70 turbines with 2.0-2.3 MW power and became operational in 2008. Ten of these WTs have a lower power of 2.0 MW. It is though unclear which turbines it regards (Pigge, 2017). There are several smaller isolated WTs in the province. Satellite images of Google Earth helped to calculate the height and rotor diameter of these WTs by using their shadow (Figure 8). The angle of the sun to the surface is dependent on the time of day and the day of year. Using the NOAA Solar calculator (NOAA, 2018) it is possible to determine the angle of the sun at the specific moment that the satellite or aerial image is taken. The height of the WT tower $h$ is given by:

$$h = \tan(\alpha)\, h' \tag{3}$$

Here $h'$ is the length of the shadow and $\alpha$ is the angle of the sun with respect to the surface. When the picture is taken in a favourable moment, with one blade oriented parallel to the tower, the length of the blade and thus the rotor diameter can be determined. Information on the height of the tower and the rotor diameter makes it possible to determine the type of WT. In many cases it was possible to determine the brand using Google Maps street view pictures. Power specifics of the WT could often

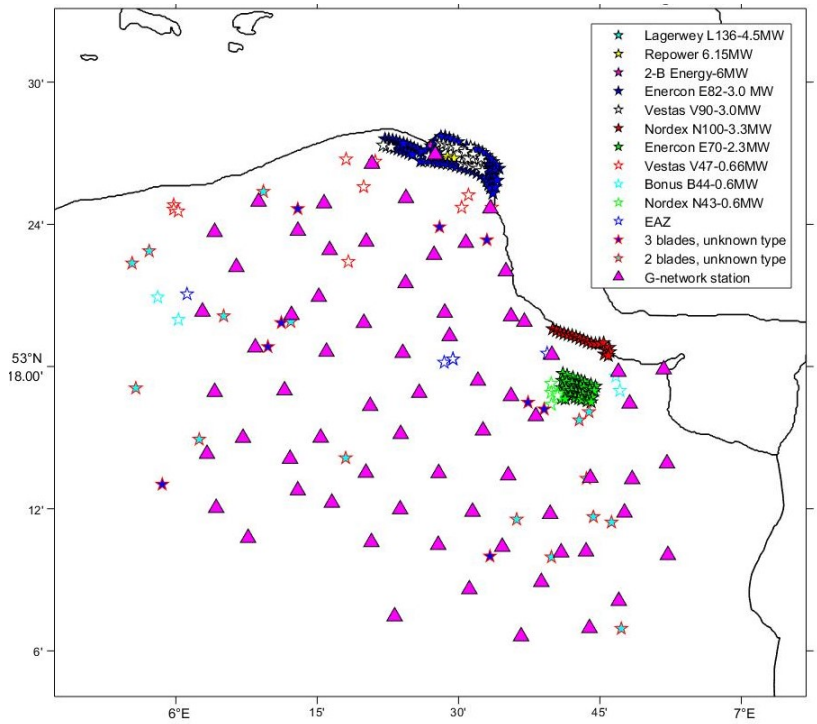


Figure 5: Distribution of WTs and G-network stations. Filled green stars indicate Delfzijl South wind park and filled red stars Delfzijl North wind park. Eemshaven wind park is located in the top north of the provice.

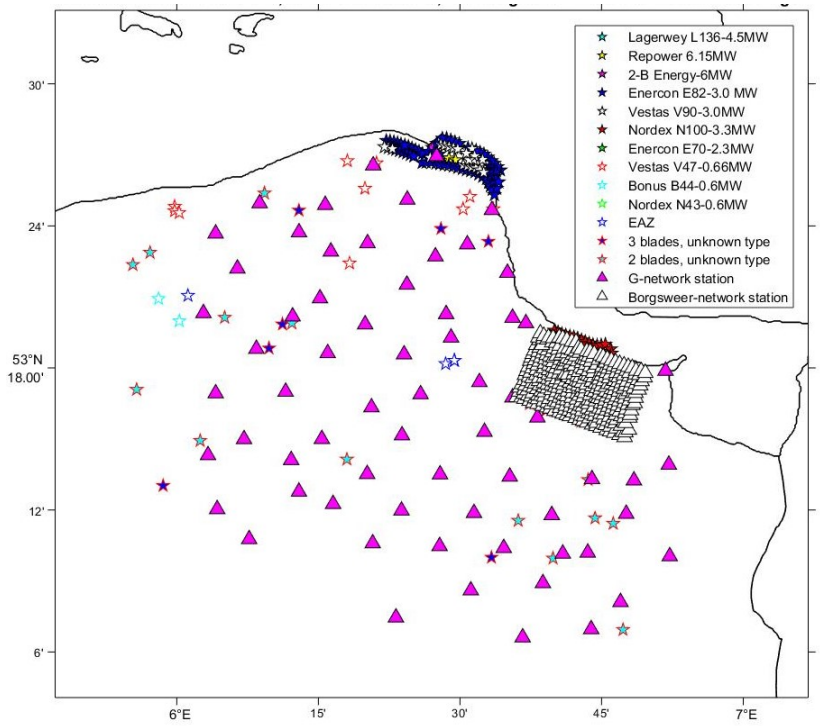


Figure 6: Distribution of the Borgsweer network in relation to the WTs and the G-network stations.

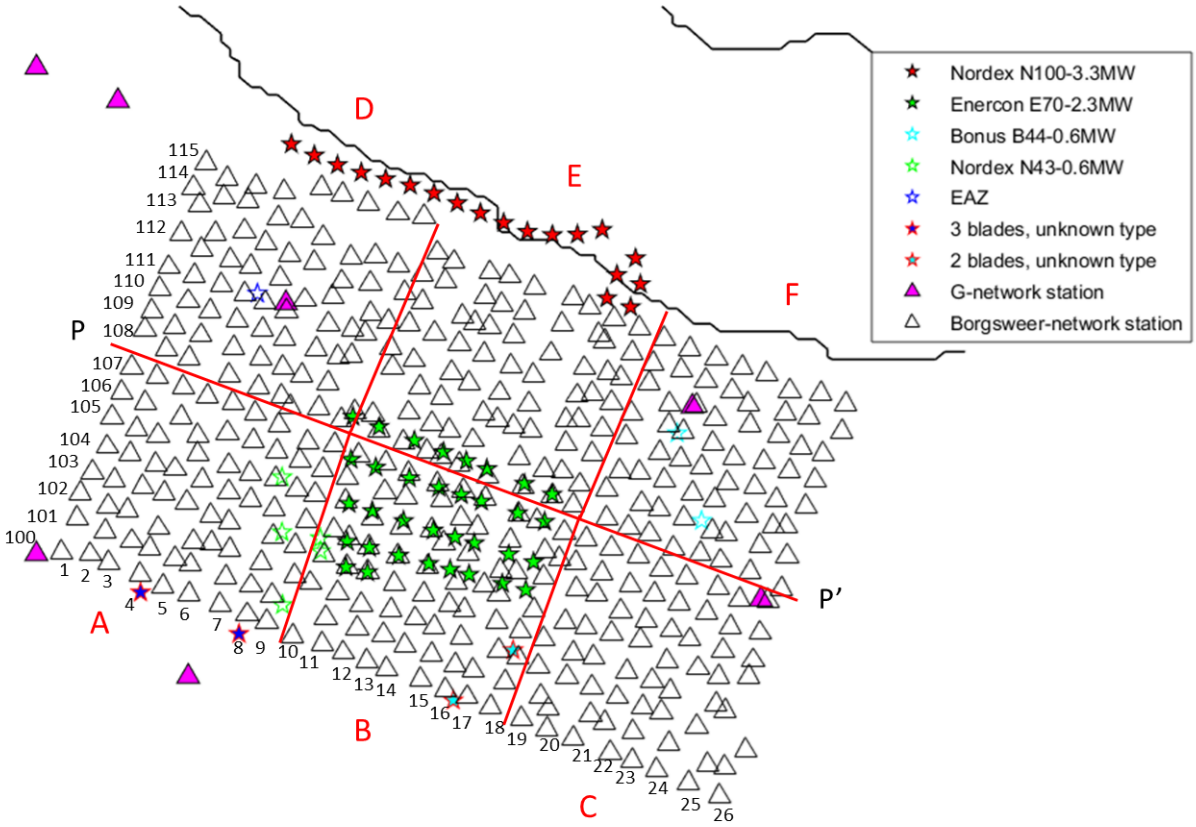


Figure 7: Distribution of Borgsweer stations, G-network stations and WTs in the Borgsweer area. Row and column numbers are indicated along the array. The calculation patches are indicated in red.

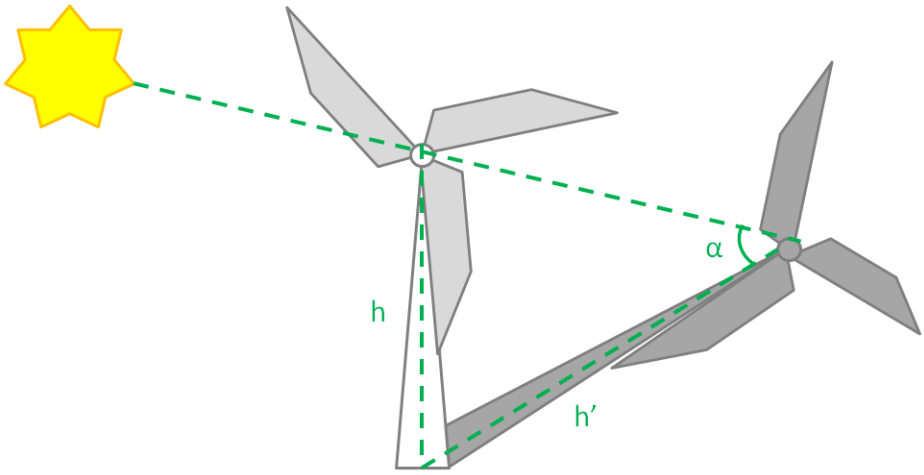


Figure 8: Schematic setup for calculating the height of a WT tower using its shadow and the angle of the sun.

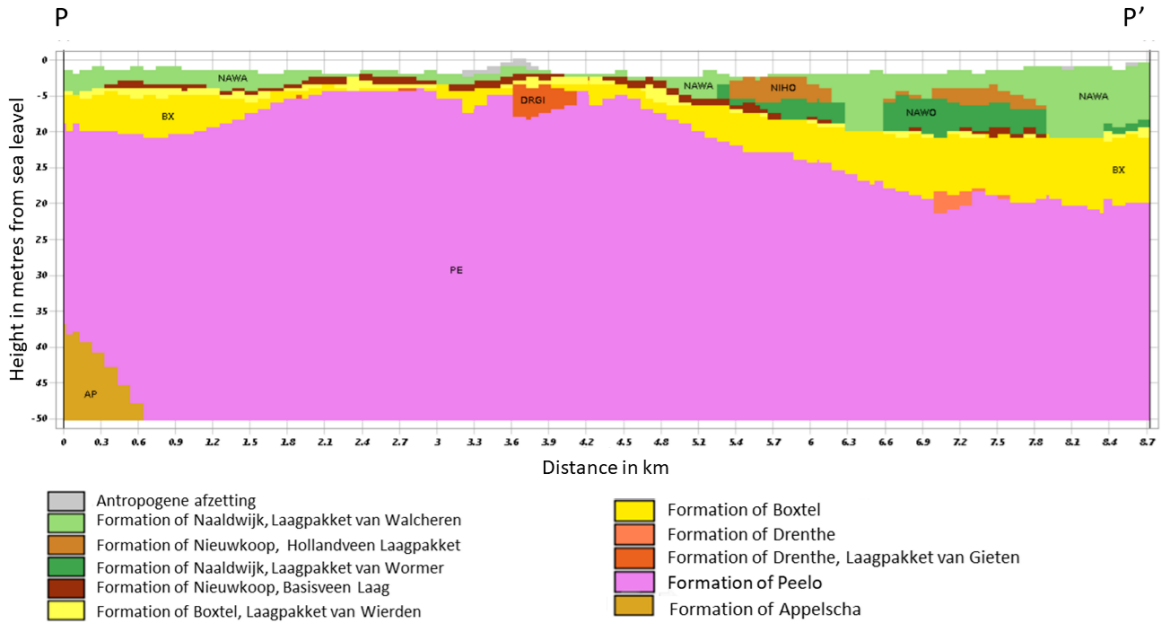


Figure 9: Cross section until 50 metres depth using the GeoTop model (Stafleu et al., 2012) obtained from TNO (2016). P and P' refer to the section line in Figure 7.

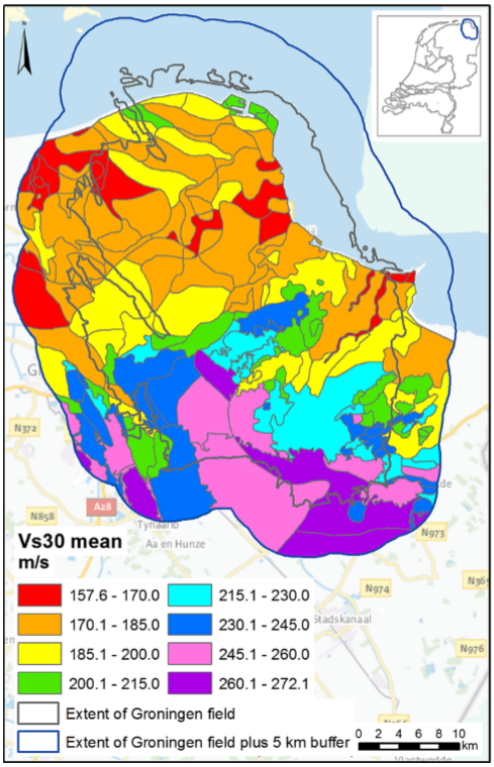


Figure 10: Mean velocity over the top 30 metres depth for the Groningen area (Kruiver et al., 2017)

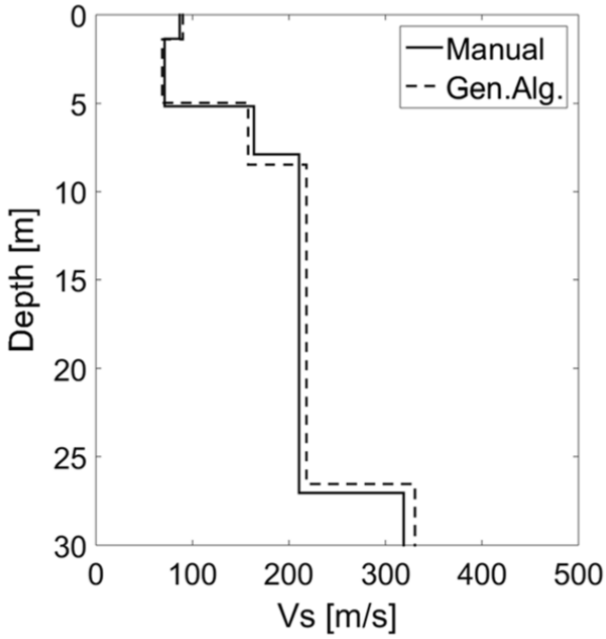


Figure 11: Velocity profile for the top 30 metres of the subsurface, taken 15 km west of the Borgsweer array. The result by manual optimisation is given by the solid line and the one using the genetic algorithm is represented by the dashed line (Noorlandt et al., 2018).

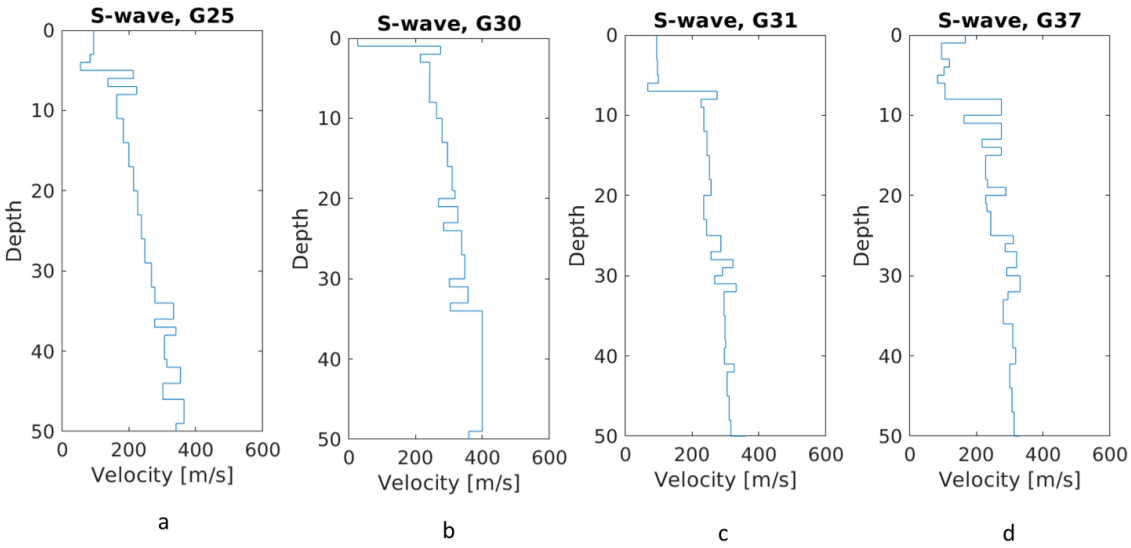


Figure 12: Velocity profiles for the G-network station (a) G25, (b) G30, (c) G31, and (d) G37 (Kruiver et al., 2017). In Figure 7, G25 can be found in patch D, G30 just south of patch A, G31 in patch F, and G37 in patch C.

be obtained using the brand and the height of the WT. The full specifics of the WTs in Groningen can be found in the Appendix.

The Borgsweer flexnet array includes the Delfzijl South wind park. The Delfzijl North wind park is close to the array (Figure 6). The dense spacing of the instruments gives a high resolution and the possibility to detect sources that attenuate fast with distance. Since the source (WT) is so close to the receiver, the wavefield is assumed to be circular. This is an advantage since beamforming of a circular wavefield can be used to find locations of the sources, in contrast to only the back azimuth that plane wave beamforming produces. According to the literature in section 1.2.3, the signal should not attenuate completely before reaching the receivers over this distance.

The attenuation and the radiation pattern of the seismic waves are strongly dependent on the properties of the subsurface. The hypothesis is that WTs mostly emit surface waves, based on the literature in section 1.2.4. In beamforming the frequency of 2.1 Hz will be used, since this frequency contains a high WT-related power (Jagt, 2017). Based on Kruiver et al. (2017) and Noorlandt et al. (2018) the velocity for this frequency is assumed to be approximately 200 m/s. This means that the wavelength is 100 metres, since wavelength is velocity over frequency. The depth sensitivity of the wave is roughly a third of the wavelength, which is in this case 33.3 metres. We will discuss geological and velocity profiles down to 50 metres depth to cover the depth sensitivity of the most important surface waves.

It is important to have some knowledge about the geology of the area to be able to explain the outcomes of the study. The GeoTop model of the The Geological Survey of the Netherlands gives a good description of the subsurface till 50 metres depth (Stafleu et al. (2011), Stafleu et al. (2012)). A cross section of the Borgsweer area over the line P/P' in Figure 7 is obtained using TNO (2016) (Figure 9). The Peelo formation is the most dominant formation and is very close to surface in the northwest of the section and relatively far from the surface in the southeast of the section. The Peelo formation consists mainly of sand and clay and is related to the extending glaciers during the Elstrien (TNO, 2013). These glaciers made gullies that were later filled up with sediments. The Boxtel formation is the second most abundant and consists mainly of sand and loam (TNO, 2013). The formation of Nieuwkoop, Hollandveen Laagpakket, consists of peat and the formation of Naaldwijk, Laagpakket van Wormer, consists of sand (TNO, 2013).

Several studies tried to find the propagation velocity for Rayleigh waves in the Borgsweer subsurface. Kruiver et al. (2017) found average velocities of 157.6-200 m/s over the top 30 metres and mapped these in Figure 10. Noorlandt et al. (2018) developed a velocity model for the top 30 metres of the subsurface, 15 km west of the array (Figure 11). This curve shows a large range of possible propagation velocities: approximately 75-315m/s. Deltares (Kruiver et al., 2017) built a S-wave velocity model for Groningen to a depth of 800 metres. Profiles from this model below the G-network stations located within our array are displayed in Figure 12. These profiles estimate a propagation velocity of 50-325 m/s. There are large variations in the top 30 metres, indicating a heterogeneous subsurface. This heterogeneous subsurface might cause large dispersion.

# 2 Method

The objective of this research is to characterize seismic signals of individual WTs in the Borgsweer area. In order to find parameters that describe the signal, a spectral analysis needs to be conducted. To untangle the individual signal from the signal of multiple WTs two steps are needed: I) finding the local combined WT signal by producing power-spectrum densities (PSDs), and II) using a cross-correlation beamforming algorithm to localize the individual WTs. The PSDs can be used to determine the attenuation pattern and the radiation characteristics as a function of wind speed and direction. A dispersion curve is constructed to estimate the travel times of the seismic waves to optimize the beamforming. A synthetic test is developed to test the working and allowed errors of the beamforming algorithm.

## 2.1 Power Spectrum Densities

Characterizing the seismic signal of WTs starts with identifying the emitted frequencies. Power spectrum densities (PSDs) are made to quantify constant emitting sources. A PSD gives the power of the signal as a function of frequency. In case of power increase at a certain frequency as a function of decreasing distance to the WT, the frequency is most likely related to the WT movement. Likewise, power will increase with increasing wind speed on WT-related frequencies, which results in an increased signal-to-noise ratio. In case of blade-rotation peaks it is possible that the power peak shifts slightly to a higher frequency, due to faster rotation of the blades. This effect is though minimized by the gearbox. Eigenmode peaks will hypothetically stay at the same frequency but increase in power. Using only the vertical component of the seismic recording is enough for these identifying WT-related frequencies. However, the three component array is needed to determine the type of seismic wave. When using all the horizontal components in a PSD as a function of wind directions, it is possible to determine the change in power with changing wind direction for both components. The ratio of the power on the different components indicates the dominating particle movement and thus reveals the type of wave.

The PSDs are calculated over small data segments of 82 seconds. The low frequency trends are removed. A Hanning window is applied to the result to give a more clear peak of the standout data points when transferred to the frequency domain. This transfer is necessary in order to be able to separate all frequencies and compute their power. In order to get ground acceleration from ground velocity, the data in the frequency domain is multiplied with the angular frequency $\omega = 2\pi f$. The PSD is computed using Equation 3 of McNamara and Buland (2004):

$$P(\omega) = \frac{1}{m} \sum_{i=1}^{m} |d_i(\omega) \cdot \omega \cdot dt \cdot df|^2 \tag{4}$$

Here $df$ is a normalization factor for the duration of the time segments ($T$). $df = 1/T$. $dt$ is the duration of a sample in seconds. $d_i(\omega)$ is the Fourier transform of the data segment $i$. The result for all segments is summed and divided by the amount of segments $m$. Squaring gives a power measure.

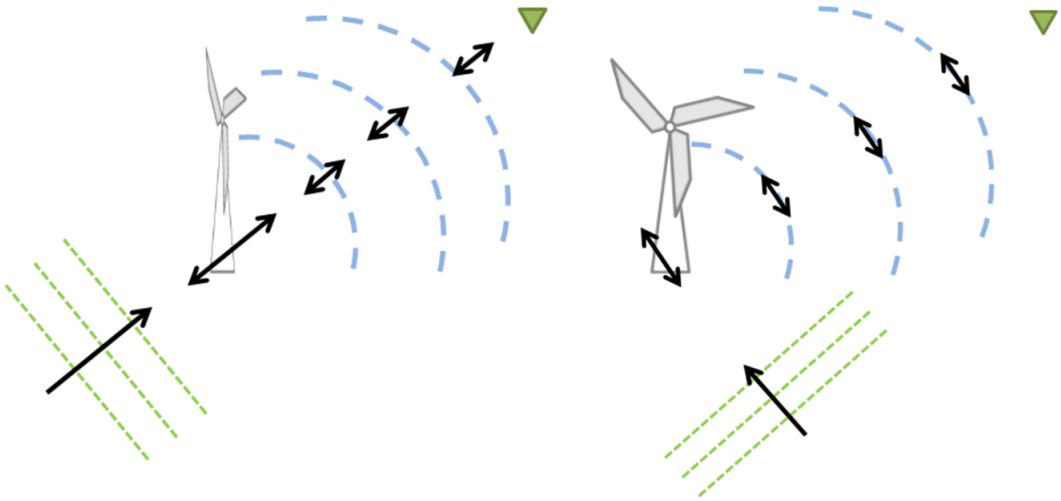

Figure 13: Setup for using wind direction to determine the seismic radiation pattern of a WT.

PSDs will be made with varying distance to the WT, varying wind speed, and varying wind direction. The first two will give a good indication of WT-related frequencies. The latter can be used to distinguish the type of waves. Figure 13 shows how the radiation pattern of the WT can be determined. One wind turbine and one station are taken at fixed locations. With varying wind directions, either Love waves, Rayleigh waves, or a combination of the two should be recorded. By taking the ratio of the power of Rayleigh versus Love waves, the radiation pattern of the WT will become clear. The horizontal components of the recording need to be decomposed into radial and transverse components, since the direction of the WT to the station will not be exactly 0, 90, 180, or 270 degrees. A weak point is that the wind direction bins are not corrected for wind speed in this study. This means that high power at a certain frequency is not solely due to the type of wave, but can also be due to increased wind speed.

## 2.2 Beamforming

The local combined WT signal is constructed from the PSDs. This provides information about the dominant frequencies emitted by the WTs. The next step is to use a cross-correlation beamforming (CCBF) algorithm to localize the individual WTs. The CCBF is chosen over the conventional beamforming, because less data is needed as input. The construction of the algorithm will be explained in detail starting from the conventional variant in the time domain assuming a plane wave and working towards the cross-correlation beamforming for point sources in the frequency domain.

### 2.2.1 Conventional beamforming

The signal-to-noise ratio (SNR) of a seismic signal can be improved by using an array and summing the seismic signals (Schweitzer et al., 2002). This will emphasize the coherent peaks and reduce the influence of incoherent noise. To conserve the amplitude of the seismic signals, the summation trace is divided by the number of traces that are summed up. It is possible to first filter the data on a certain frequency (band) and solely get the arrivals of that frequency. Due to different locations of the instrument sites with respect to the source, some signals will be delayed in relation to the signals of other instruments. Correcting for the delay time is therefore necessary to get a consistent outcome of the summing. Delay times $\tau_j$ of instrument $j$ are defined as projection of the position vector $\bar{x_j}$ of instrument $j$ onto the slowness vector $\bar{s}$ (Schweitzer et al., 2002). Each slowness describes one plane-wave model.

$$\tau_j = \bar{x_j} \cdot \bar{s} \tag{5}$$

This is logical since the delay is dependent on the propagation velocity over the surface and the distance over the surface it has to travel. The propagation velocity over the surface is called the apparent horizontal velocity. Apparent velocity is the velocity of the wavefront measured in a certain direction. Apparent horizontal velocity and velocity are related by the sine of the angle at which the wavefront approaches the receivers (Figure 14a):

$$v_{a,h} = v \sin(i) \tag{6}$$

The angle of incidence is indicated by i. Since the seismic waves emitted by WTs are assumed to be surface waves, and therefore $i$ is 90 degrees, $\sin(i) = 1$ and the assumption is that the velocity is equal to the apparent velocity. The apparent velocity can be decomposed in two components: the north and the east velocity component (Figure 14b). The inverse of the apparent velocity is called the slowness and is given by:

$$\bar{s} = [s_E, \ \ s_N] = [\frac{1}{v_E}, \ \ \frac{1}{v_N}] \tag{7}$$

Since the Borgsweer area does have no significant elevation, a 2D horizontal plane is assumed and the vertical component is not taken into account. The time delay is the distance from the source to the receiver divided by the apparent velocity. Thus the measured wavefield is compared to the plane wavefield, since the slowness vector includes information about this plane wavefield. Using the time delays, the data $d$ of the seismometers at site $j$ and time $t$ can be summed and divided by the amount of traces $N$. This gives the beam $b$ of the signal:

$$b(t) = \frac{1}{N} \sum_{j=1}^{N} d_j(t + \bar{x_j} \cdot \bar{s}) \tag{8}$$

We are interested in the beam power $B$. To obtain power, the absolute values of the summation should be squared, which yields an energy measure:

$$B(t) = \frac{1}{N} |\sum_{j=1}^{N} d_j(t + \bar{x}_j \cdot \bar{s})|^2 \tag{9}$$

To be able to execute the beamforming for a certain frequency $f$, the work needs to be done in the frequency domain. Following Ruigrok et al. (2017), first the data is taken to the frequency domain:

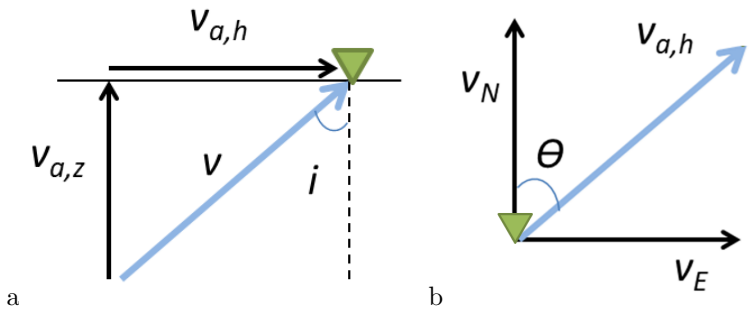


Figure 14: a) Side view: the blue arrow indicates a plane wave propagating with a velocity $v$. The velocity vector can be decomposed in an apparent horizontal and vertical velocity. Velocity and apparent velocity relate through the angle of incidence $i$.b) Top view: the blue arrow indicates the apparent horizontal velocity with back azimuth $\theta$. This component can be decomposed in a north velocity component ($V_N$) and an east velocity component ($V_E$).

$$D(\bar{x}_j, \omega) = \int_{-\infty}^{\infty} d(\bar{x}_j, t) e^{-i\omega t} dt \tag{10}$$

The angular frequency is given by $\omega = 2\pi f$. Just like in conventional beamforming, the data is multiplied by the delay times and then summed. The delay times are taken into the frequency domain.

$$B(s, \theta, \omega) = \frac{1}{N} |\sum_{j=1}^{N} D(\bar{x}_j, \omega) e^{i\omega \, \bar{x}_j \cdot \bar{s}}|^2 \tag{11}$$

The slowness vector $\bar{s}$ can be written differently:

$$\bar{s} = [s_E, \ s_N] = s[\sin(\theta), \ \cos(\theta)] \tag{12}$$

Here $\theta$ is the back azimuth and $s$ the horizontal slowness.The equation for beamforming can be rewritten to take into account the definition of the wave vector $\bar{k}$, which contains information about the plane wave model.

$$\bar{k} = [k_E, \ \ k_N] = \frac{\omega}{\bar{v}} = \omega \cdot \bar{s} = \omega \ s[\sin(\theta), \ \ \cos(\theta)] \tag{13}$$

$$B(s, \theta, \omega) = \frac{1}{N} |\sum_{j=1}^{N} D(\bar{x}_j, \omega) e^{i\bar{x}_j \bar{k}^{\ T}}|^2 \tag{14}$$

The delay times are now defined as the position vector times the wave vector $\bar{k}$.

### 2.2.2 Cross-correlation beamforming

Conventional beamforming works well for a regularly spaced array. When the array is not regularly spaced, like in Figure 15, the illumination along line A will be much better than then along line B. This is due to the fact that the stations along line A have many different time delays and the stations along line B all have the same time delay. This gives aliasing: i.e. spurious repetitions of the beampower related to the actual direction of the signal. Birtill and Whiteway (1965) found that a mitigation to this problem would be to cross-correlate the data. By cross-correlating the data from a station along line A to a station along line B the empty space between the lines is covered.
Furthermore, after cross-correlating the data it is possible to take certain receiver pairs out. This means that station pairs that are in the same line can be taken out, so that the line will not be over-illuminated. The result will be more reliable with less aliasing. Auto correlations can be left out, since they only add non-information and therefore make the important information less clear (Ruigrok et al., 2017). Even though this study has a relatively regularly spaced array, the results of beamforming will improve using CCBF due to the removal of autocorrelations. Ruigrok et al. (2017) showed that the CCBF algorithm provides better resolution, less aliasing, and better resilience to non-coherent noise with respect to the conventional beamforming algorithm. Since the output of this research should be a very detailed map in which the beampower of the WT stands out, this more precise method will be used. CCBF will here be explained after Ruigrok et al. (2017). Cross-correlation of the data in the frequency domain is expressed as:

$$C(\bar{x}_i, \bar{x}_j, \omega) = D(\bar{x}_i, \omega)\{D(\bar{x}_j, \omega)\}^* \tag{15}$$

The beampower can then be calculated by:

$$B(s, \theta, \omega) = \frac{1}{N} |\sum_{m=1}^{N} C_m(\omega) e^{i\omega 2 h_m p \cos(\theta_m - \theta)}| \tag{16}$$

Here $h_m$ are the half offsets, $\theta_m$ are the receiver-pair azimuths, $N$ is the amount of receivers, and $m$ is a receiver-pair index. Note that no squared norm is taken here, since the cross-correlation of the data

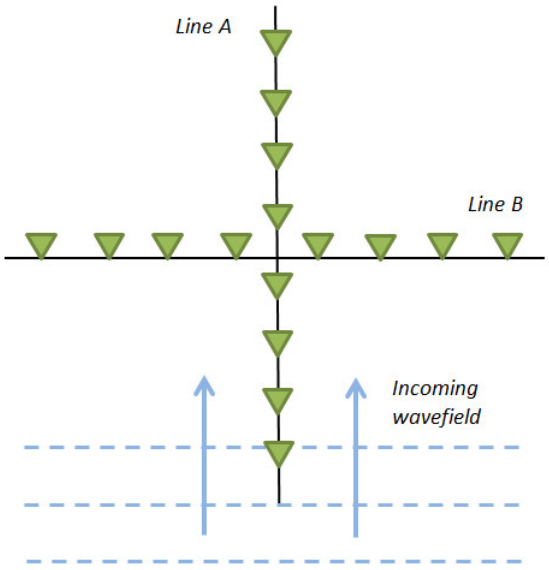


Figure 15: 20 element symmetrical cross array after Birtill and Whiteway (1965)

already yields an energy measure (Ruigrok et al., 2017). Ruigrok et al. (2017) showed that applying phase shifts prior to cross-correlation is similar to applying phase shifts after cross-correlation. Since the intention is to use the algorithm for a narrow frequency band, instead of a certain frequency, with varying signal strength over this bandwidth, it is useful to use the cross-coherence instead of the cross-correlation. The cross-coherence $C_{coh}$ is a spectrally-normalized cross-correlation:

$$C^{coh}(\bar{x}_i, \bar{x}_j, \omega) = \frac{D(\bar{x}_i, \omega)\{D(\bar{x}_j, \omega)\}^*}{|D(\bar{x}_i, \omega)||D(\bar{x}_j, \omega)|} \tag{17}$$

The slowness vector is the inverse of the velocity and will therefore vary with different types of waves, subsurface, and directionality. In this study the velocity is unknown.

A plane wave is assumed during the process described above. This means that the distances from the source to the receiver are larger than approximately four or five times the array aperture (Almendros et al., 1999). This is not the case for this setup, since the distance from source to receiver is always smaller then one time the array aperture. Therefore the kernel of the time delay will have to be rewritten for a point source approach. With a plane wave model it is not possible to map the exact location of the beampower, since there is no information about the start time $t_0$, but only about the direction $\theta$ of the incoming wave. On the contrary, a circular waveform yields information about how far the wave has travelled, based the gradient of the wavefront. Therefore it will be useful to change the wave model to a circular wavefront coming from a point source. This will yield a change to the Cartesian coordinate system, which is convenient for mapping beampower.To find an exact location, the time $t_0$ needs to be taken out of the equation. This can be done by making a kernel out of the cross-correlation of displacement of the expected waves in the frequency domain. The arrival of a wave $u_1$ at the receiver $i$ can be written as:

$$u_i = A_i e^{i\omega t_i} = A_i e^{i\omega(r_i/v)} \tag{18}$$

Here $A_i$ is the amplitude at receiver $i$ and $r_i$ is the distance from the source to receiver $i$ ($r_i = |\bar{x}_s - \bar{x}_i|$) (Figure 16). Consequently, $A_j$ is the amplitude at receiver $j$ and $r_j$ is the distance from the source to receiver $j$ ($r_j = |\bar{x}_s - \bar{x}_j|$). Cross-correlation with the arrival at instrument $j$ gives:

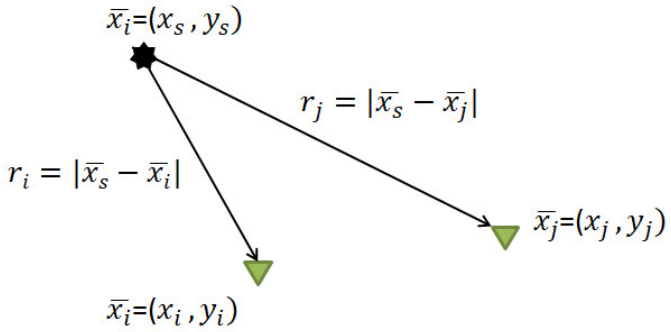


Figure 16: Setup for cross-correlation of displacement at two instruments: $i$ and $j$.

$$u_i^* u_j = A_i A_j e^{-i\omega(r_i/v)} e^{i\omega(r_j/v)} \tag{19}$$

$$u_i^* u_j = A_i A_j e^{i\omega(r_j - r_i/v)} = A_i A_j e^{i\omega(r_{ij}/v)} \tag{20}$$

Since the amplitude is normalized when calculating the beampower, this term can be neglected. The e-factor is a kernel for beamforming, since it contains information about the circular wavefront. It can now be used to calculate the exact location of the source, since exact distances are involved in contrast to direction vectors. With $\omega = 2\pi f$, this results in the following final equation for beampower:

$$B(s, \theta, \omega) = \frac{1}{N} | \sum_{m=1}^{N} C_m^{coh}(\omega) e^{i2\pi f(r_{ij}/v)} | \tag{21}$$

Here $r_{ij}$ is the distance difference between $r_i$ and $r_j$. When divided by the velocity, this gives the time delay between instrument $i$ and $j$.

A narrow frequency band can be taken for the chosen frequency $f$. The narrower the band, the more precise the result will be. Therefore the result might get better by dividing the frequency band in multiple frequency bins. This way new cross-coherence data will be taken for every frequency bin and after beamforming all of the results are added up. Beamforming will then more clearly display the sources and show less aliasing.

The sampling rate of the signal is 5 Hz. This means that the Nyquist frequency, the frequency that still represents the signal well, is 2.5 Hz. Beamforming above 2.5 Hz will therefore give unreliable results. Only the recorded Z-components are used for beamforming, since the WT signal on this component is expected to be strong enough.

## 2.3 Dispersion curves

During beamforming a 'guessed' velocity will be inserted to map beampower. This process is trial and error based. When the velocity is accurate, the highest beampower for the chosen frequency peak should be at the location of the WTs. Therefore it is very convenient to know what the dispersion curve for the area is. A dispersion curve relates frequency to velocity. The basic idea is that the dispersive properties of the subsurface are used to determine a phase velocity for every frequency. Since the Z-component is used in beamforming, the dispersion curve will also be calculated for the Z-component of the recorded signal.

The way of establishing the dispersion curve is after Park et al. (1998). Here the mathematical steps of his method will be followed and explained. His Multi-channel Analysis of Surface Waves (MASW)

will give the velocity properties of the subsurface. The process of calculating a dispersion curve starts with using a Fourier transform to bring the data into the frequency domain and to decompose it into individual frequency components. The Fourier transform is taken of the offset-time $(x-t)$ domain representation $d(x,t)$ of a shot gather:

$$D(x,\omega) = \int d(x,t)e^{-i\omega t}dt \tag{22}$$

All frequencies are separated. $D(x,\omega)$ can be written as a multiplication of a phase term and an amplitude term:

$$D(x,\omega) = P(x,\omega)A(x,\omega) \tag{23}$$

$P(x,\omega)$ is the phase spectrum and contains the arrival time information. Thus, the dispersion properties are given by this term. $A(x,\omega)$ is the amplitude spectrum and contains information on attenuation and spherical divergence. The $P(x,\omega)$ term can also be expressed as $e^{-i\Phi x}$ in which $\Phi = \frac{\omega}{c_\omega}$. The frequency in radians is given by $\omega$ and $c_\omega$ is the phase velocity for this frequency. This gives the final expression for $D(x,\omega)$:

$$D(x,\omega) = e^{-i\Phi x}A(x,\omega) \tag{24}$$

To each component an amplitude normalization is applied. $D(x,\omega)$ is divided by its absolute value. The phase velocity $c_\omega$ ranges from 100 to 2000 m/s. For every $c_\omega$ the required phase shifts are calculated to correct for time delay for a specific offset. Finally, the components are summed to calculate the energy. This integral transformation is applied as follows:

$$V(x,\phi) = \int e^{-i\phi x}[D(x,\omega)/|D(x,\omega)|]dx \tag{25}$$

$$V(x,\phi) = \int e^{-i(\Phi-\phi)x}[D(x,\omega)/|D(x,\omega)|]dx \tag{26}$$

From this outcome maximum energies can be picked for a specific frequency. The steps are repeated for every frequency. The maximum energy indicates the phase velocity for the given frequency. The maximum $V(x,\phi)$ for a given $\omega$ will be found when $\phi = \Phi = \frac{\omega}{c_\omega}$, since $A(x,\omega)$ is real and positive. For a value of $\phi$ with a certain peak of $V(x,\phi)$, the phase velocity $c_\omega$ can be determined (Park et al., 1998). The dispersion curve is a line that connects all highest energies in the diagram. A high energy connects frequency to phase velocity. It is possible that multiple points with high energy show at one frequency due to higher modes. The different modes can then be distinguished from each other by picking multiple maxima (Park et al., 1998). This method differs from the basic method of McMechan and Yedlin (1981) in the way that first the field record is placed in the frequency domain and afterwards a slant-stack is applied. McMechan and Yedlin (1981) started with the slant-stack and afterwards transferred to the frequency domain. The advantage of the method of Park et al. (1998) is that higher modes are better displayed. This is useful since in this study higher modes are expected to show at the low frequencies.

## 2.4 Synthetic test

A synthetic test is used to test the reliability of the beamforming method. In this test sources are chosen manually and seismic waves are forward modelled. The response is turned into a noise response to come as close to the real seismic signal as possible. First a source wavelet is created that is convolved with the Green's function. A transient source would only be active for a short amount of time, but noise sources like WTs emit seismic waves continuously. The signal is convolved with random noise to resemble a noise source. The amplitude of the signal is normalized to obtain an increased signal-to-noise ratio. The subsurface is assumed to be homogeneous and has a constant velocity $v_{real}$. The test is developed to test the working of the algorithm and to test the effect of I) the position and number of sources within the array on mapping of the sources, II) applying a cross-coherence or a cross-correlation to the data, III) applying the cross-coherence before or after transferring the data to

the frequency domain, IV) the frequency of the emitted wave, V) the velocity of wave propagation, and VI) a velocity error between $v_{real}$ and the modelled velocity $v_{mod}$. The latter velocity is the velocity used for beamforming.

### 2.4.1 The effect of the position and number of sources within the array on mapping of the sources

The presence of multiple sources might have as effect that some sources are less focused and have a weaker beampower than other sources after mapping. Sources that are positioned central in the array are expected to have a higher beampower than sources that lie at the border of the array, because less instruments will pick up a significant signal from a source at the border than from a source at the centre of the array.

To start out, one source was placed at the centre and later at the border of the array. $v_{real} = v_{mod} = 0.5$ km/s and the dominant frequency is 1 Hz. The frequency band of beamforming is 0.95-1.05 Hz and this band is divided in 4 frequency bins. A cross-coherence is applied to the data before taking it to the frequency domain. Figure 17a shows that the source in the centre of the array is mapped very well. When the source is placed at the border of the array (Figure 17b), the location is less precise due to a lack of azimuthal coverage. Sources that lie more central in the array will therefore be mapped more precisely.

When beamforming the response of 16 simultaneously acting sources, some sources give a stronger result than others. In general, all sources can be mapped (Figure 18). Mainly sources at the border of the array are less focused and have a lower beampower. Interference of sources and resonance of the subsurface is not taken into account.

### 2.4.2 The effect of applying a cross-coherence or cross-correlation to the data

The theoretical advantage of a cross-coherence is described in section 2.2.2. To confirm the theory, the test for 16 sources was repeated with a cross-correlation of the data in contrast to the cross-coherence executed before. Other variables are not changed. It is clear that the sources are more focused when beamforming with a cross-coherence of the data (Figure 18a) in contrast to a cross-correlation of the data (Figure 18b). The beampower of the sources with less azimuthal coverage is higher using a cross-coherence.

### 2.4.3 The effect of cross-cohering the data before or after taking the Fourier transform

The beamforming implementation either calculates the cross-coherence from the data itself or accepts data on which the cross-coherence (or -correlation) has already been executed. The advantage of making cross-coherences outside the beamforming program is that these can be saved and do not have to be calculated again for a new run with adjusted variables. This is very time effective. The data is then transferred to the frequency domain by the algorithm after cross-coherence. This is in contrast to the order when putting in the raw data: then the data is first taken into the frequency domain before applying the cross-coherence. The advantage of the latter is that more samples are taken into the frequency domain, since in a cross-coherence only the samples with most information are saved. This means that putting the raw data into the beamforming algorithm should give a slightly more precise result. Figure 19 shows that the result indeed differs a bit from Figure 18a, though the difference in insignificant. Some sources are illuminated or focused slightly better or less. Since the difference is small, it is convenient to calculate the cross-coherences before transferring the data to the frequency domain to save calculation time.

### 2.4.4 The effect of the frequency of the emitted wave

A wave with a higher frequency has a shorter wavelength. This means that the source location will be more precise. Previously, the dominant frequency was 1 Hz, but this will now be increased to 2.1 Hz. Jagt (2017) found this frequency to be WT-related and dominant for the Delfzijl South wind park.

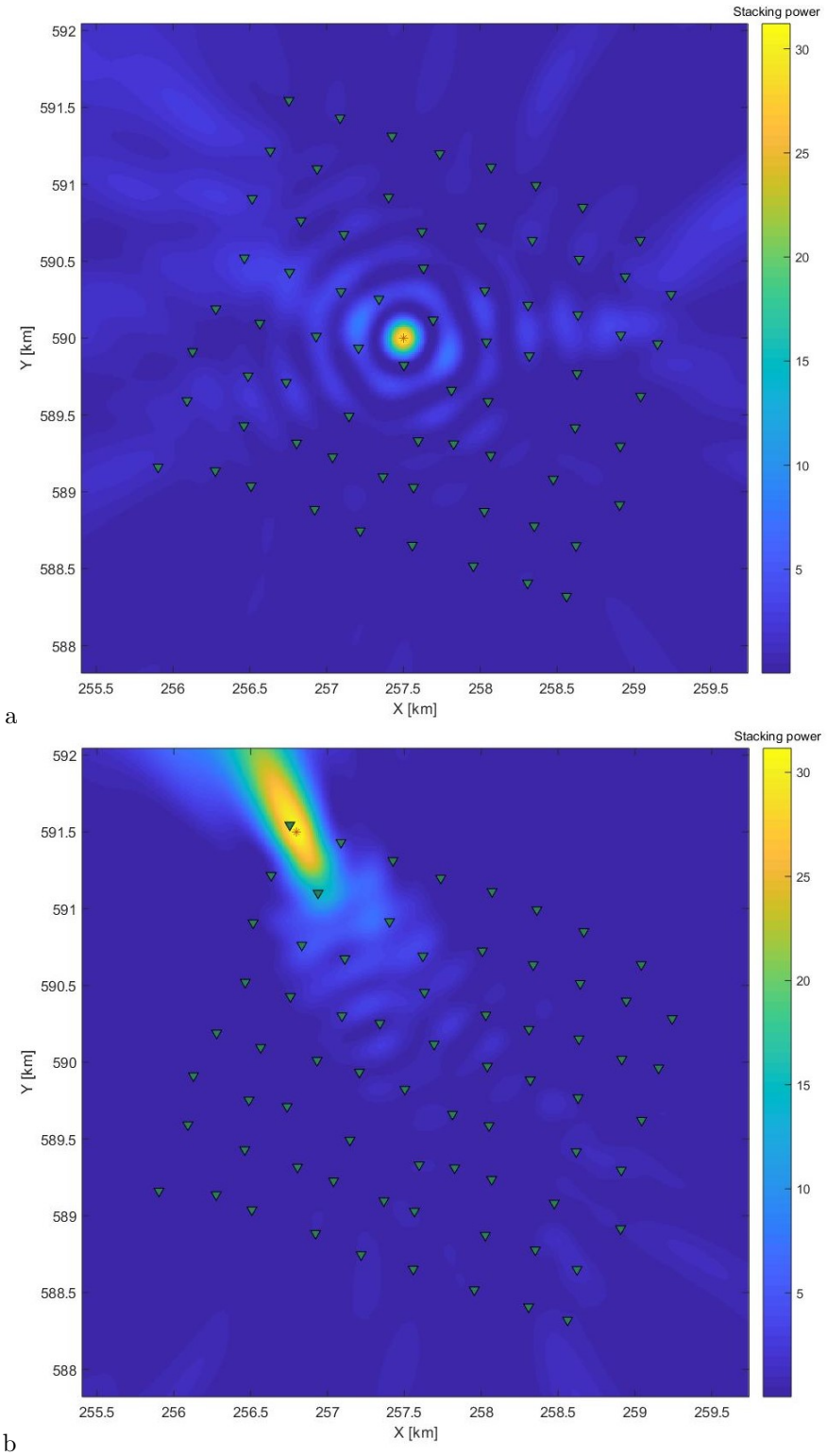


Figure 17: Mapped beampower for one source (red star) at the centre of the array (a) and the border of the array (b). Instruments are indicated by green inverted triangles. $v_{real} = v_{mod}$ =0.5 km/s, the dominant frequency is 1 Hz, and the frequency band of beamforming is 0.95-1.05 Hz divided over 4 frequency bins. A cross-coherence is applied to the data before beamforming.

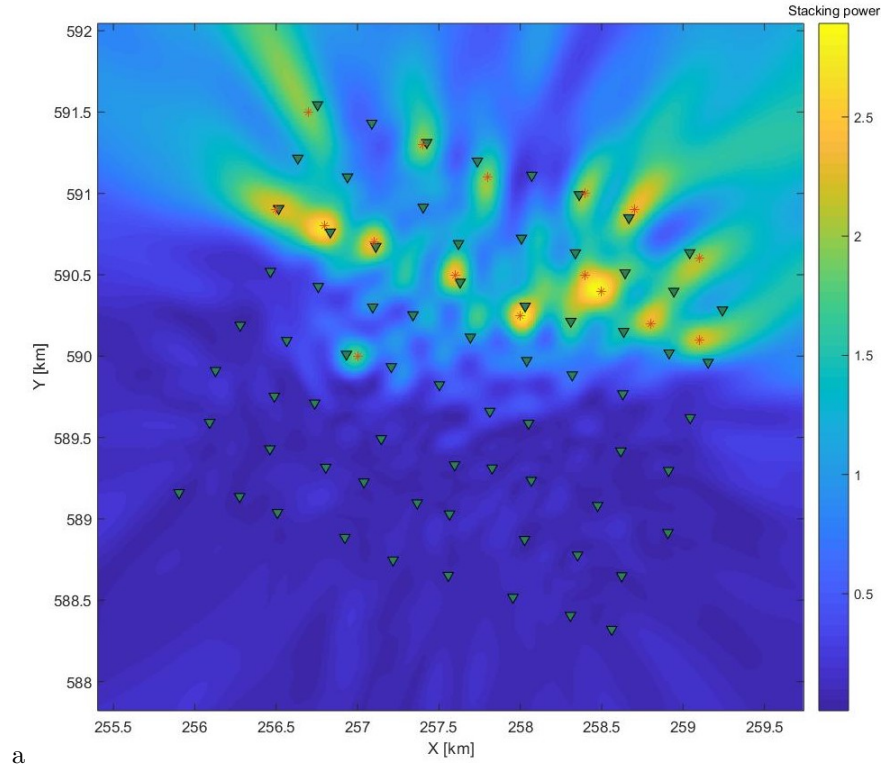


a

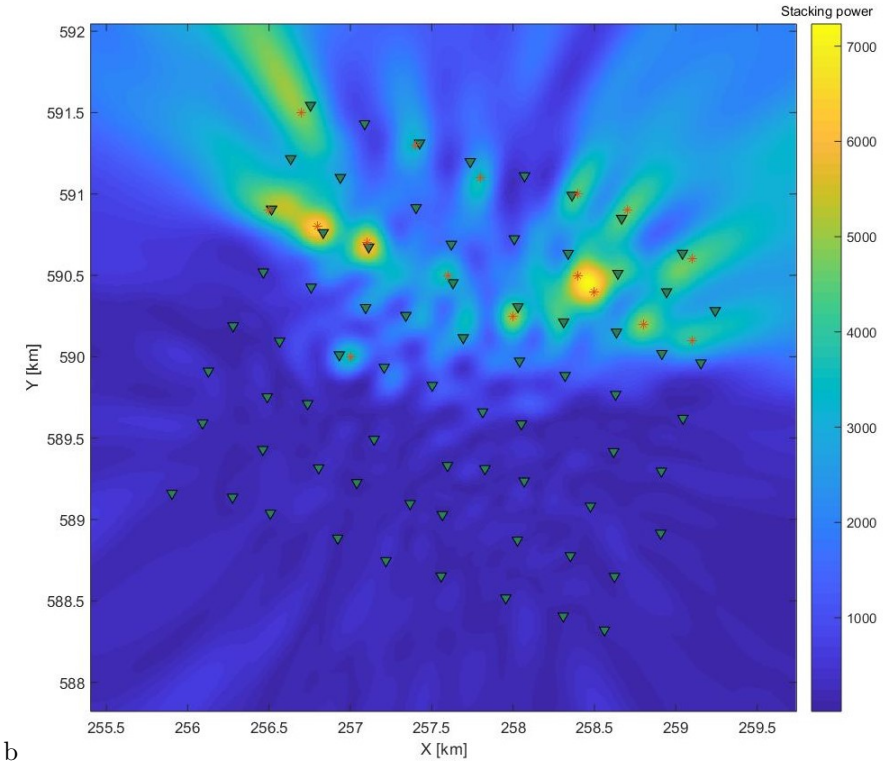


b

Figure 18: Beamforming for sixteen sources using a) a cross-coherence and b) a cross-correlation. $v_{real} = v_{mod}$ =0.5 km/s, the dominant frequency is 1 Hz, and the frequency band of beamforming is 0.95-1.05 Hz divided over 4 frequency bins.

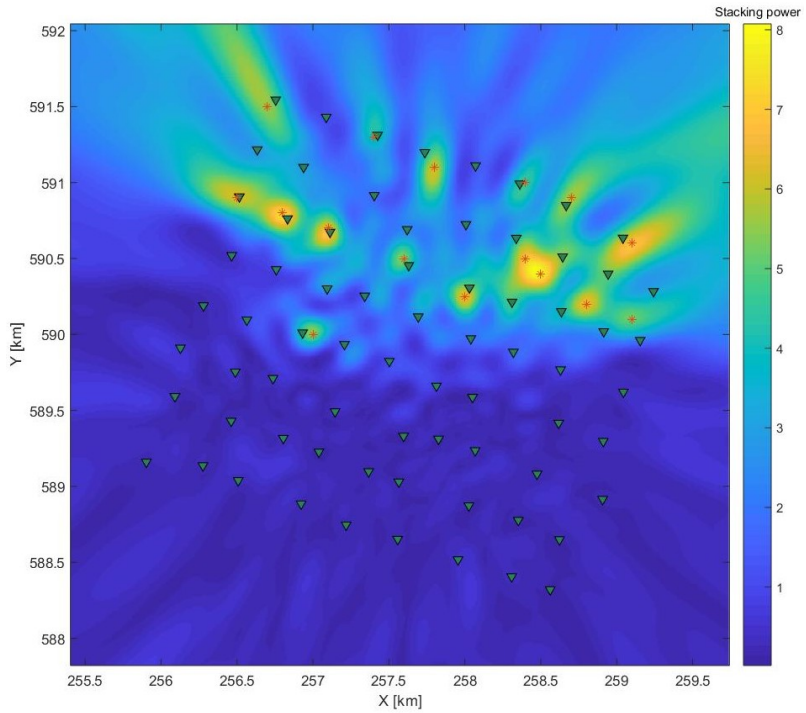


Figure 19: Beamforming for sixteen sources using a cross-coherence applied after transferring the data to the frequency domain. $v_{real} = v_{mod}$ =0.5 km/s, the dominant frequency is 1 Hz, and the frequency band of beamforming is 0.95-1.05 Hz divided over 4 frequency bins.

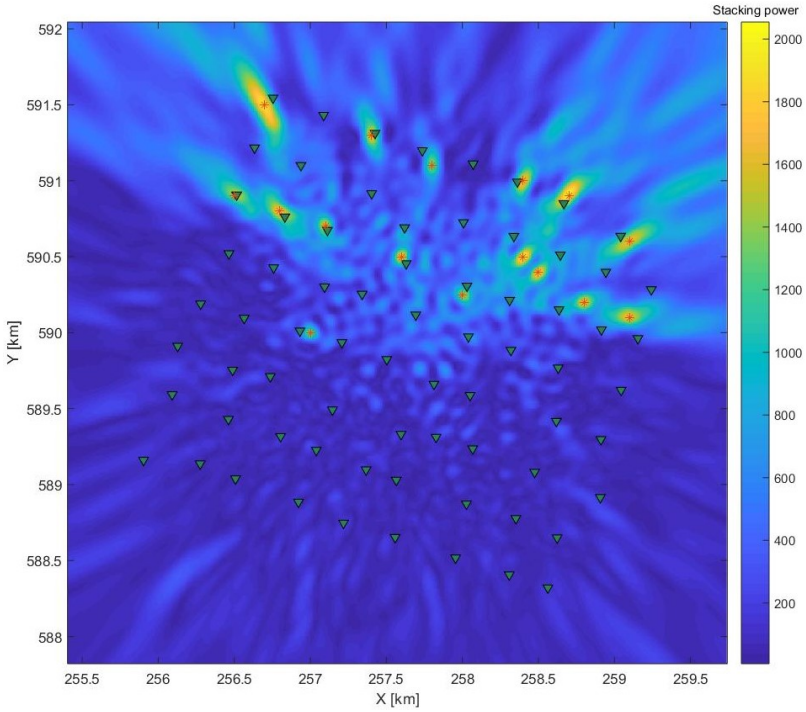


Figure 20: Beamforming for sixteen sources using a cross-coherence. $v_{real} = v_{mod}$ =0.5 km/s, the dominant frequency is 2.1 Hz, and the frequency band of beamforming is 2.05-2.15 Hz divided over 4 frequency bins.

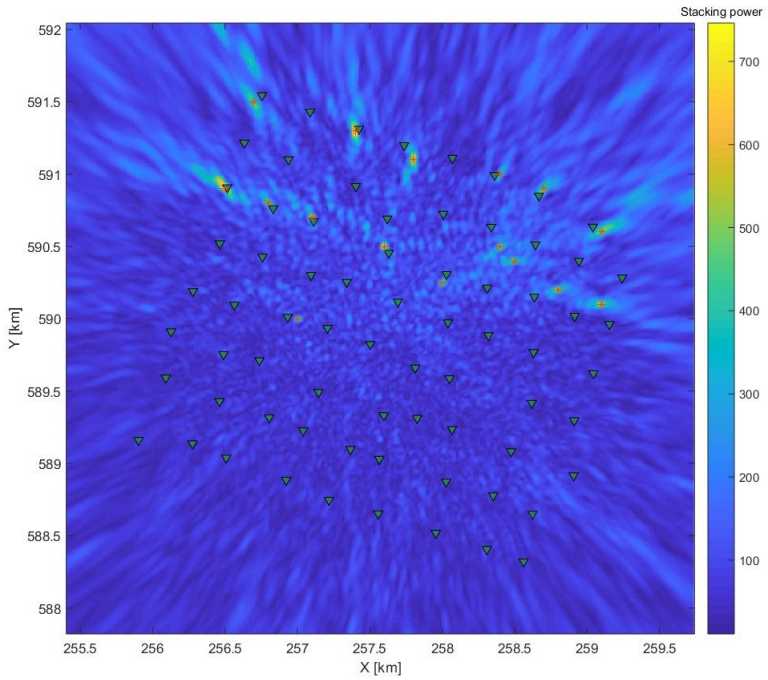


Figure 21: Beamforming for sixteen sources using a cross-coherence. $v_{real} = v_{mod}$ =0.25 km/s, the dominant frequency is 2.1 Hz, and the frequency band of beamforming is 2.05-2.15 Hz divided over 4 frequency bins.

Figure 20 shows that the sources indeed are localized more precisely when the frequency increases to 2.1 Hz. The sources become smaller in surface area, which makes it possible to distinguish between sources that are located closely to each other.

### 2.4.5 The effect of the velocity of wave propagation

The propagation velocity of waves has an effect on the number of wavelengths the instruments will receiver within a certain time. A lower velocity will lead to less information and therefore a lower beampower. A reasonable speed for a 2.1 Hz frequency is about 0.15-0.3 km/s for the top 30 metres (Noorlandt et al. (2018), Kruiver et al. (2017)). The test is repeated for a velocity of 0.25 km/s (Figure 21), which is more realistic for 2.1 Hz. The result shows clearly that the sources are strongly reduced in size. The low velocity will make it difficult to map the WTs with real data. It is possible to enhance the localization of the sources at low speeds by convolving the result with a Gaussian function if needed.

### 2.4.6 The effect of a velocity error between the real velocity $v_{real}$ and the modelled velocity $v_{mod}$

The velocity is guessed for the WT signal during beamforming. When the right $v_{mod}$ is filled in, the sources should be at the locations of the WTs. It is useful to know what the maximum velocity error is to still locate the source at the location of the WT. This experiment is done with a realistic velocity of 0.25 km/s for a frequency of 2.1 Hz. For a velocity $v_{real}$ of 0.25 km/s, the modelled velocity $v_{mod}$ can range from 0.242 km/s (Figure 22a) to 0.258 km/s (Figure 22b). This is a variation of plus and minus 3.2%.

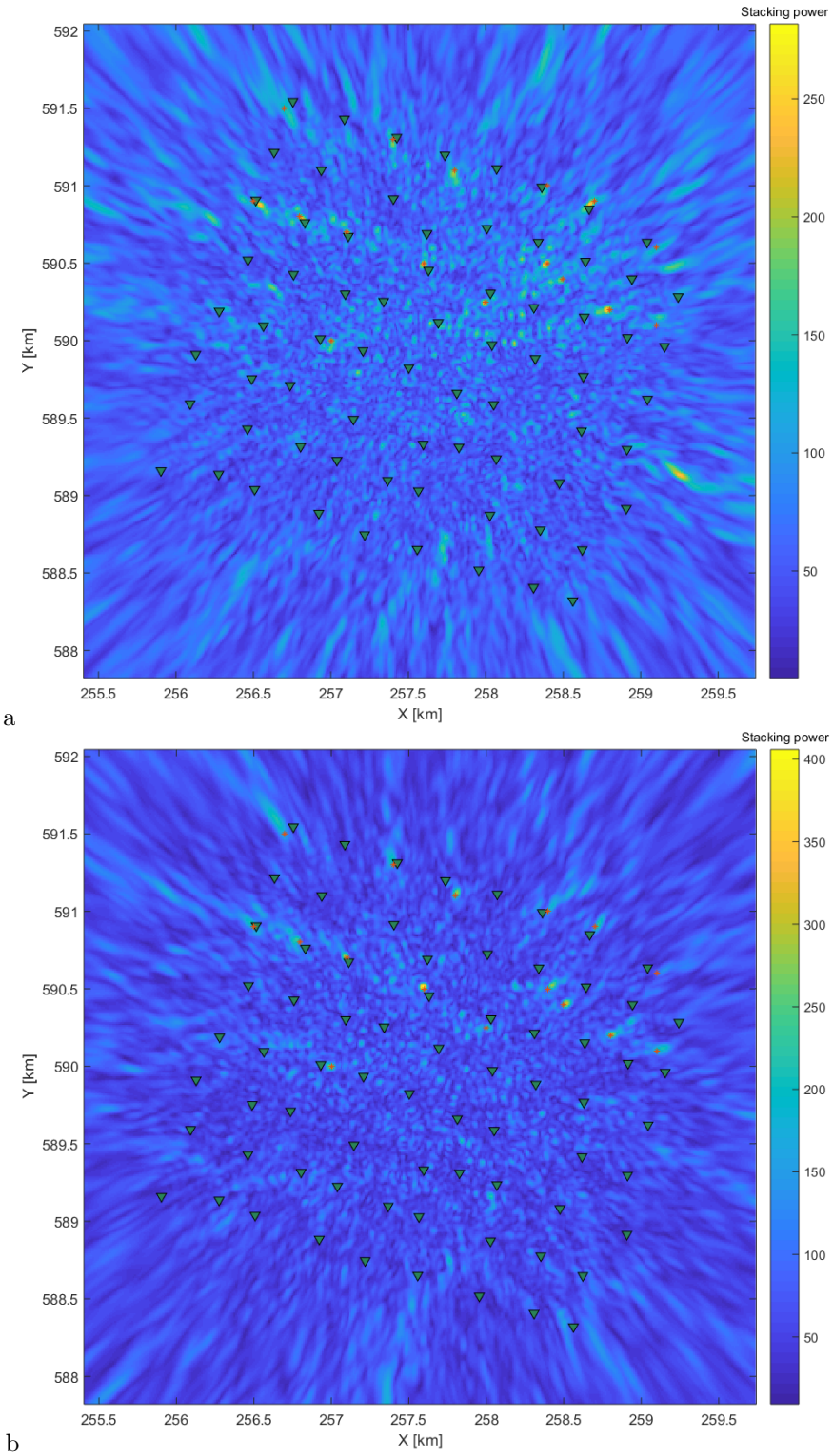


Figure 22: Beamforming for sixteen sources using a cross-coherence. $v_{real} = 0.25km/s$, the dominant frequency is 2.1 Hz, and the frequency band of beamforming is 2.05-2.15 Hz divided over 4 frequency bins. a) $v_{mod}$ =0.242 km/s, b) $v_{mod}$=0.58 km/s.

# 3 Results

## 3.1 Local combined WT signal

### 3.1.1 Recording compatibility

First a noise recording of the Borgsweer array is compared to that of the G-network by comparing a 1-day PSD. Two sensors at approximately the same position are used: sensor G310, which is an accelerometer at zero metres depth, and 113.21 (Figure 23). The distance between the sensors is approximately 30 metres. Day 12 of 2017 is chosen as input data for this comparison due to its moderate wind speed conditions. The PSDs match closely between 0.25 and 3 Hz. This means that the correction for the instrument response is adequate compared to the G310 sensor. The G310 sensor with these settings is used and verified in Dost et al. (2017).

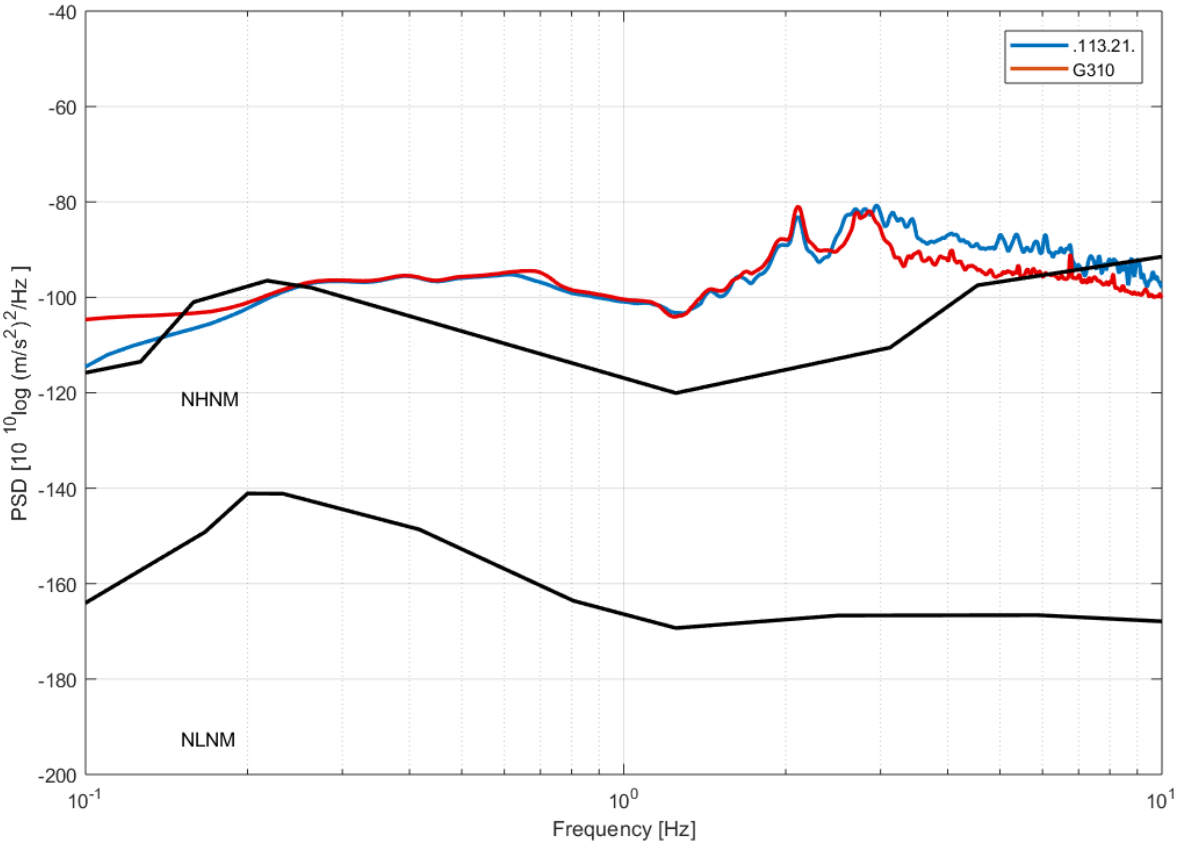


Figure 23: PSD of day 12, 2017, showing a G-network station (G310) and a Borgsweer network station (113.21). Both stations are placed at the surface. NHNM stands for the new high noise model and NLNM stands for the new low noise model (Peterson et al., 1993).

### 3.1.2 PSD with varying distance to the WTs

To determine which frequencies are emitted by the WTs, PSDs are produced with varying distance to the WTs. When the distance to the WT decreases, the power at WT generated peaks should increase.

To test the effect of varying distance to the WTs on power, a PSD is made of all stations in row 7 of the array. Figure 24 shows the stations that are used. The color scale of the row indication matches the colors of the resulting PSDs in Figure 25. The PSDs show a clear increase in power with shorter distance to the Delfzijl South wind park for the frequencies 2.1, 3.0, 4.6, 6, 7.4, and 9.3 Hz. It is clear that the power overall increases with decreasing distance to a WT and that the power at most frequencies lies above the NHNM (new high noise model) of Peterson et al. (1993).

### 3.1.3 PSDs with varying wind speed

In addition, WT-related frequencies can be identified by making PSDs for varying wind speeds. Increasing wind speed should lead to an increase in power of WT-related peaks. It is interesting to look at the near-field effects of the WTs in contrast to the general WT signal of the whole array. Figure 26 shows the PSDs of varying wind speed of a station (103.12) located 15 metres from a WT of the Delfzijl South wind park. Remarkable are the two lowest frequency peaks at 0.31 and 0.63 Hz. The 0.31 Hz peak has a significantly larger power than the 0.63 Hz peak. Following the theory that a WT moves as a clamped beam (section 1.2.2), 0.63 Hz cannot be an overtone of 0.31 Hz, since the first overtone would be three times the fundamental frequency, resulting in a first overtone of 0.93 Hz. These two frequencies are therefore most likely eigenmode frequencies of two different sources. The expected overtones for these two fundamental frequencies are calculated following the physics of a standing wave on a clamped beam. For the frequency of 0.31 Hz the following overtones are expected: 0.93, 1.55, 2.17, 2.79, 3.41, 4.03, 4.65, 5.27, 5.89, 6.51, 7.13, 7.75, 8.37, 8.99, 9.61, 10.23, 10.85, and 11.47 Hz. The expected overtones for the 0.63 Hz frequency are: 1.89, 3.15, 4.41, 5.67, 6.93, 8.19, 9.45, and 10.71 Hz. These frequencies are indicated by coloured bands in Figure 26. Orange bands for the expected overtones of 0.31 Hz and blue bands for the expected overtones of 0.63 Hz. At the frequencies of most expected overtones, a peak in power is shown. Furthermore, the power increases with increasing wind speed, indicating that these frequencies are WT-related. Some peaks, like 3.41, 5.27, 6.51, and 7.75 Hz do not show a peak in power. The peak at 2.1 Hz is remarkable since it increases in frequency with increasing wind speed. In Figure 27 the difference between the 2.1 Hz peak and a stationary peak at 2.5 Hz is shown. The 2.1 Hz peak is the only peak that clearly shows an increase in frequency with increasing wind speed.

Now that the near-field signal is known, the complete signal of the array will be studied. This signal is comparable to the far-field signal. Figure 28 shows the PSD for the complete signal with varying wind speeds and indication of the expected multiple frequency peaks. Remarkable is that the frequency of 0.31 Hz and 0.93 Hz are not visible. All other expected frequency peaks are showing in the plot. There are though some frequencies with high power that are not indicated by an expected multiple band. The most important ones are 1.24, 2.5, 3.28, 3.8, and 5.05 Hz. Finally, a remarkable feature is that the peak at frequency 0.63 Hz seems to disappear with increasing wind speed.

### 3.1.4 Spatial PSDs

Spatial PSDs are created to find the spatial power pattern of certain frequencies. A few key frequencies are tested for their distribution over the array: expected eigenmode frequency 0.31 Hz and the multiple 0.93 Hz, expected eigenmode frequency 0.63 Hz and the multiple 1.89 Hz, and the rotation-related frequency of 2.1 Hz. Figure 29 shows that the 0.31 Hz frequency is only measured when the station is located very close to the WT in the Delfzijl South wind park. Furthermore, some random measurements of the frequency are shown that do not seem to be related to a WT. Near ten WTs the 0.31 Hz signal is recorded. The distribution of power at this frequency is more clear when using the N-component than the Z-component, therefore this component is chosen to make the spatial PSD. The same settings are chosen to look at the first expected multiple of 0.31 Hz: 0.93 Hz (Figure 30). The same ten stations located close to WTs of the Delfzijl South park do show high power for this frequency. Furthermore, the frequency seems to have increased power on the east side of the wind park. A slight increase in power is seen in the north of the array, close to the Delfzijl North wind park.

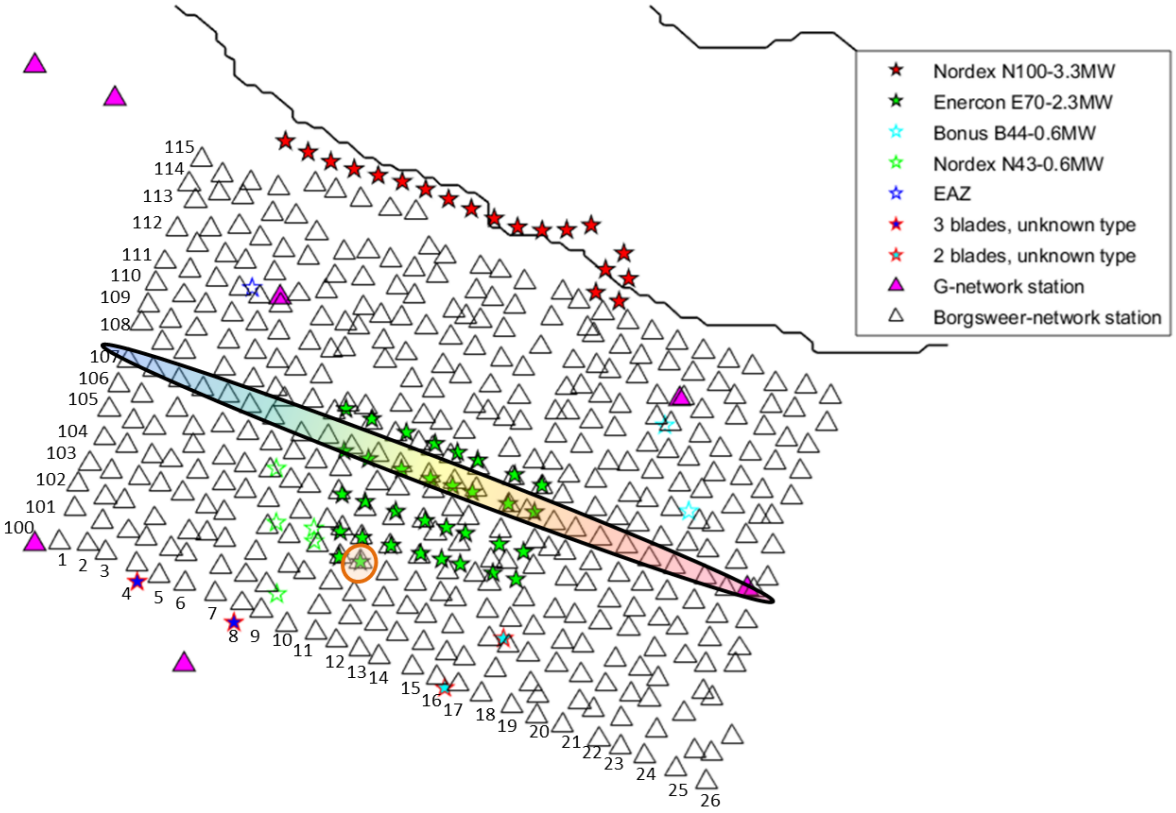


Figure 24: Indication of the stations of row 7 (black delineated ellipse) and station 103.12 (orange delineated circle). The stations of row 7 are used to make Figure 25. These stations are located at varying distances to the Delfzijl South wind park. Station 103.12 is used to make Figure 26.

.

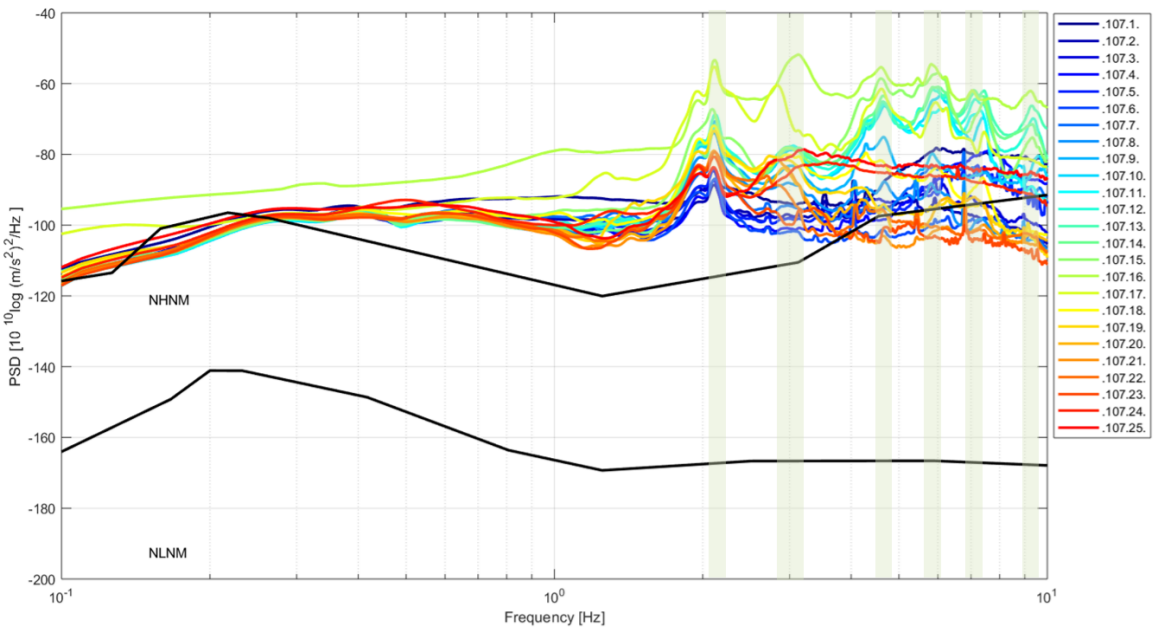


Figure 25: PSD for the Z-component of day 11, 2017, for the stations of row 7 as indicated in Figure 24. Stations 107.10 to 107.17 are located in the Delfzijl South wind park. The frequency bands with standout peaks are marked by green bands. NHNM stands for the new high noise model and NLNM stands for the new low noise model (Peterson et al., 1993).

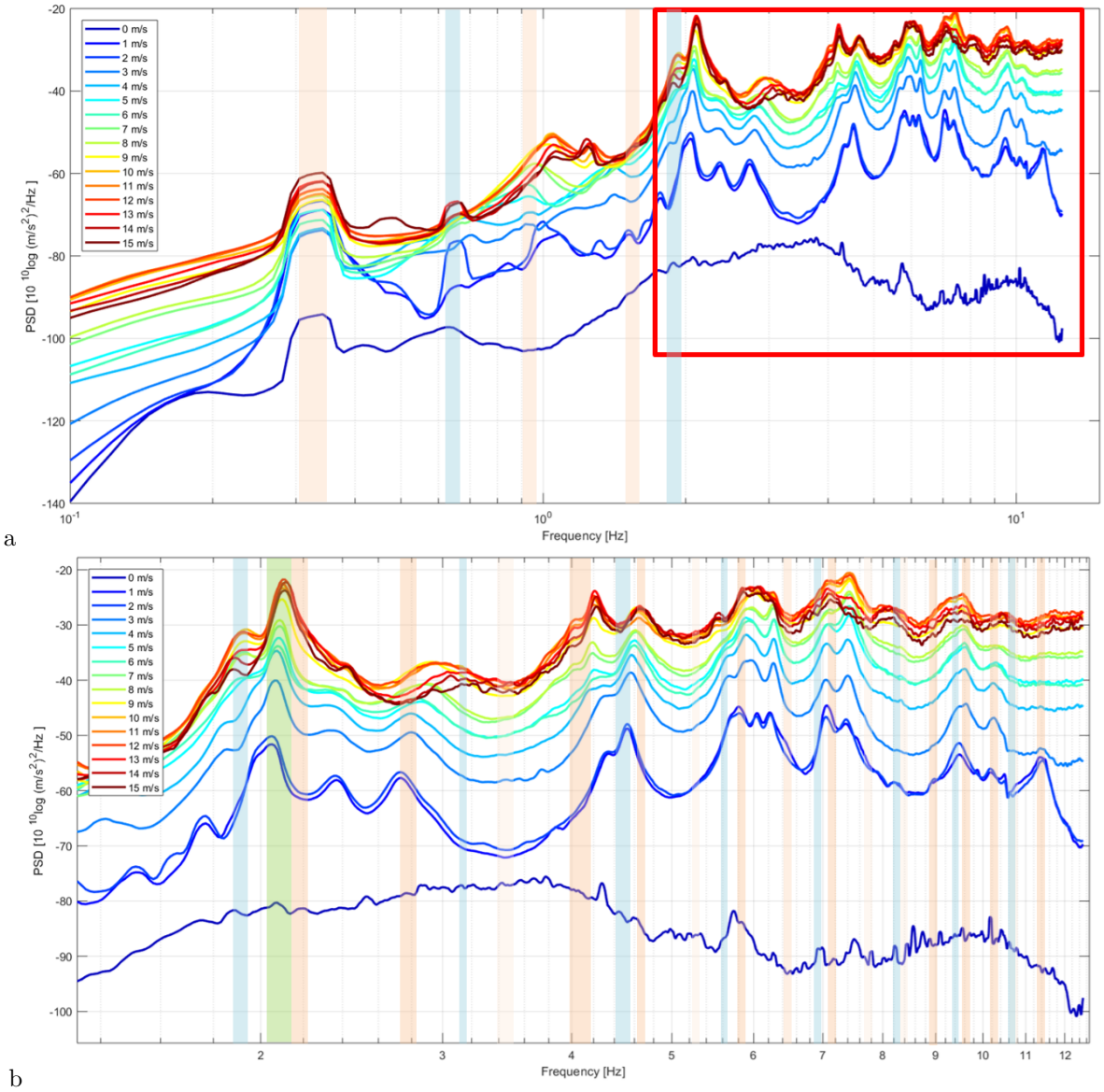


Figure 26: PSD for the Z-component of day 7-22, 2017, for station 103.12 with varying wind speed. For location see Figure 24. Orange bands indicate frequencies of multiples of the 0.31 Hz frequency. Blue bands indicate frequencies of multiples of the 0.63 Hz frequency. The green band indicates a rotation-related frequency. Figure b) is a zoom-in of the red box in Figure a).

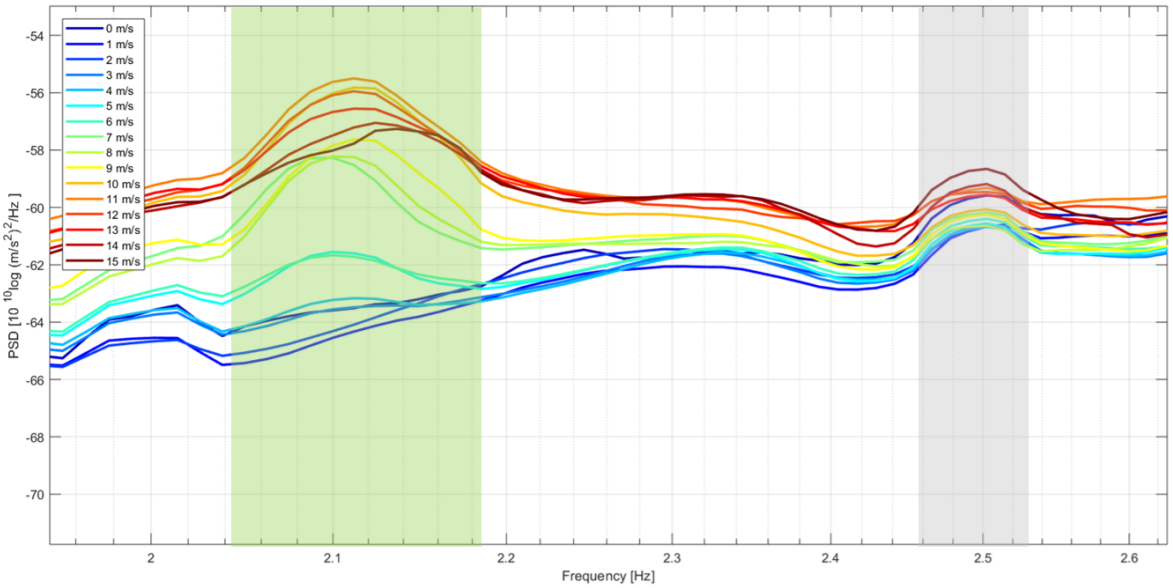


Figure 27: Example zoom-in of Figure 28 between 2 and 2.6 Hz showing the difference between a rotation-related frequency at 2.1 Hz (green band) and a stationary peak at 2.5 Hz (grey band).

The spatial PSD for the frequency of 0.63 Hz (Figure 31) shows a clear increase in power in the northwest of the array. The power levels are only slightly elevated under the Delfzijl South wind park. The expected frequency of the first overtone, 1.89 Hz (Figure 32), shows the same pattern in the northwest of the array. The plot is made for a day with low wind speeds, since eigenmode frequencies are then expected to be less overpowered by microseism.

Finally, the spatial PSD for the frequency of 2.1 Hz (Figure 33) shows a clear increase in power under the Delfzijl South wind park. Remarkable is the attenuation pattern. The signal seems to attenuate more in the west than in the east. To find an explanation for this distinct attenuation pattern, the top of the geological Peelo formation is plotted under the spatial PSD. The top of the Peelo formation is in the east found much deeper than in the west. In the east the distance between the top of the Peelo formation and the surface is filled up with sand, peat and loam sediment layers (Figure 9). The plot is made for a day with high wind speeds, since rotation-related frequencies are then expected to have a large power.

### 3.1.5 PSDs with varying wind direction

Station 101.22 is used to determine the radiation pattern of the WT in the southeast corner of the Delfzijl South park as a function of wind direction (Figure 34). Though the aim is to identify the radiation pattern of the individual WT, it is likely that the influence of the whole Delfzijl South wind park is recorded. The wind park is located at 300-347 degrees from north. When the wind direction is parallel to this direction or 180 degrees turned, a strong Rayleigh component is expected, as stated in theory section 2.1.

The PSDs of the radial (Figure 35a)and the transverse component (Figure 35b) show strong peaks for the frequencies of 0.6, 0.87, 1.89, and 2.1 Hz. The peak of 0.87 Hz has until now not been recorded with such a high power. Clearly this frequency emits a strong horizontal power and almost no vertical power. The frequency is a bit lower than the 0.93 Hz frequency found before.

Now taking the ratio of the radial over the transverse component, three peaks are standing out due to

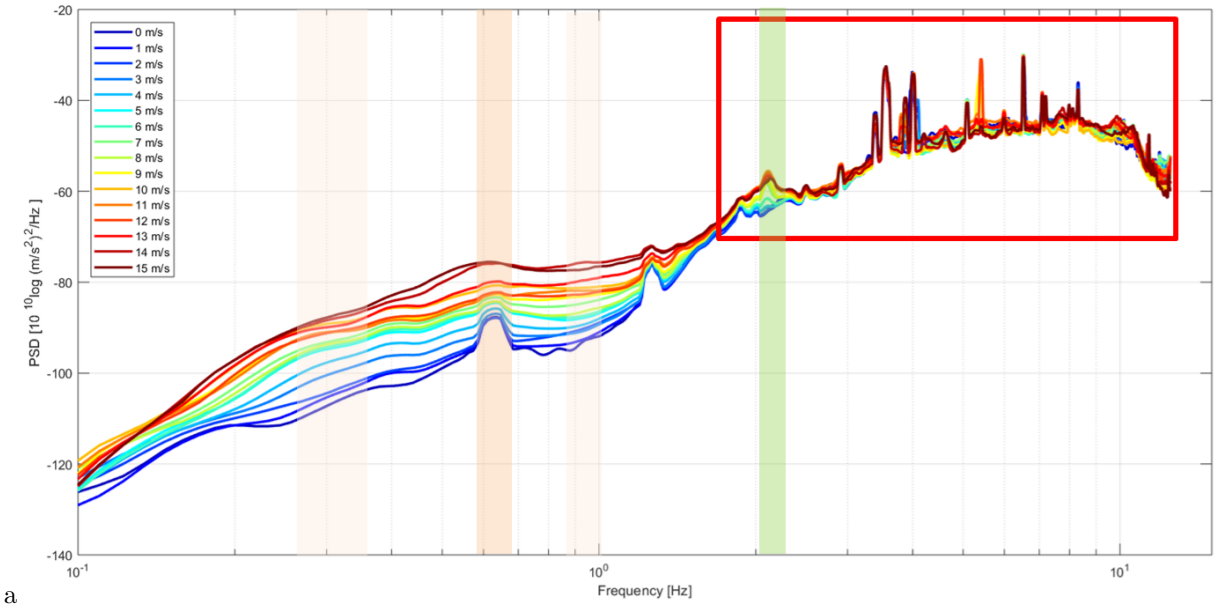


a

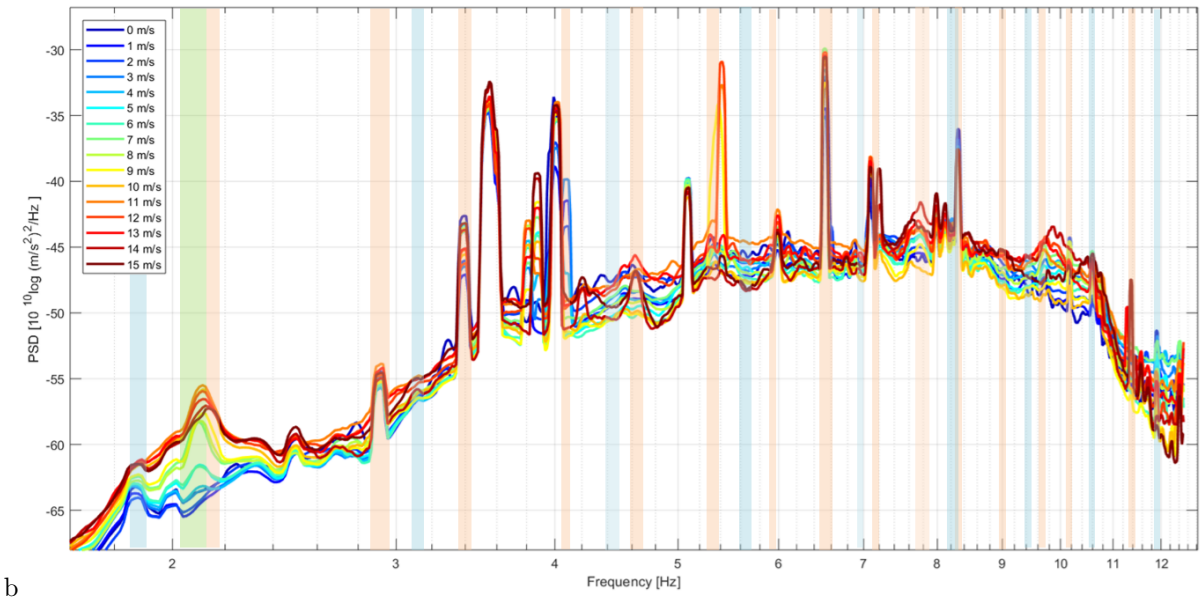


b

Figure 28: PSD for the Z-component of day 7-22, 2017 for all stations with varying wind speed. Orange bands indicate frequencies of multiples of the 0.31 Hz frequency. Blue bands indicate frequencies of multiples of the 0.63 Hz frequency. The green band indicates a rotation-related frequency. Figure b) is a zoom-in of the red box in Figure a).

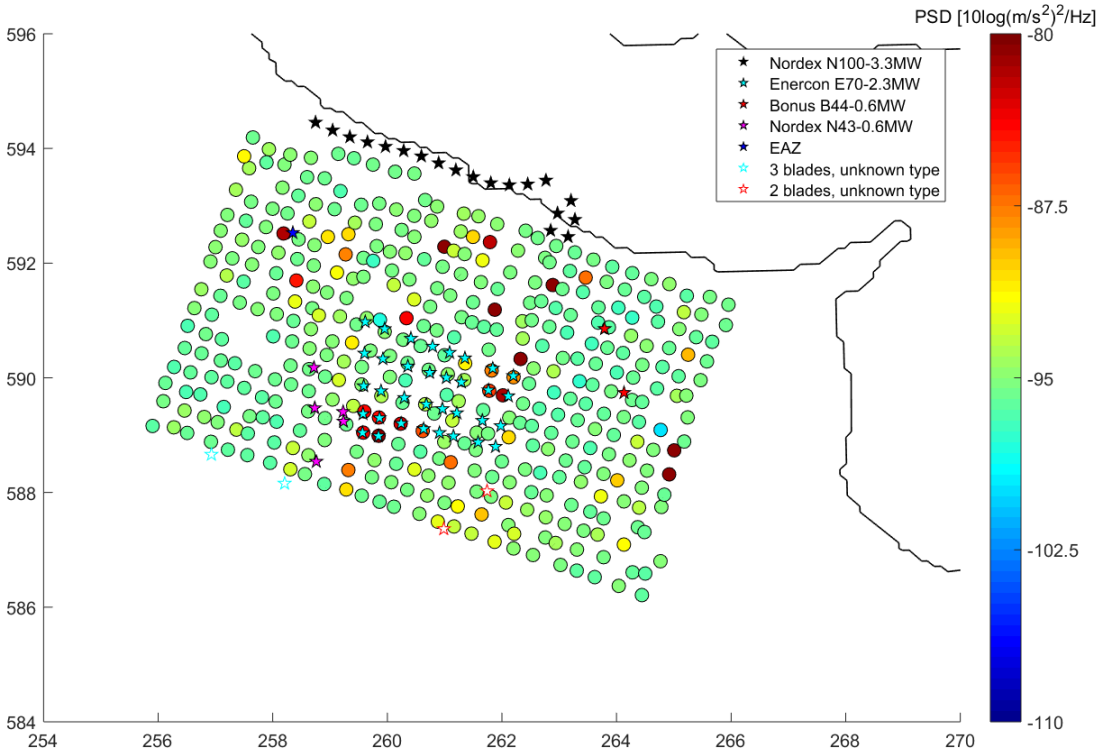


Figure 29: Spatial PSD for the frequency of 0.31 Hz of the N-component during day 11, 2017.

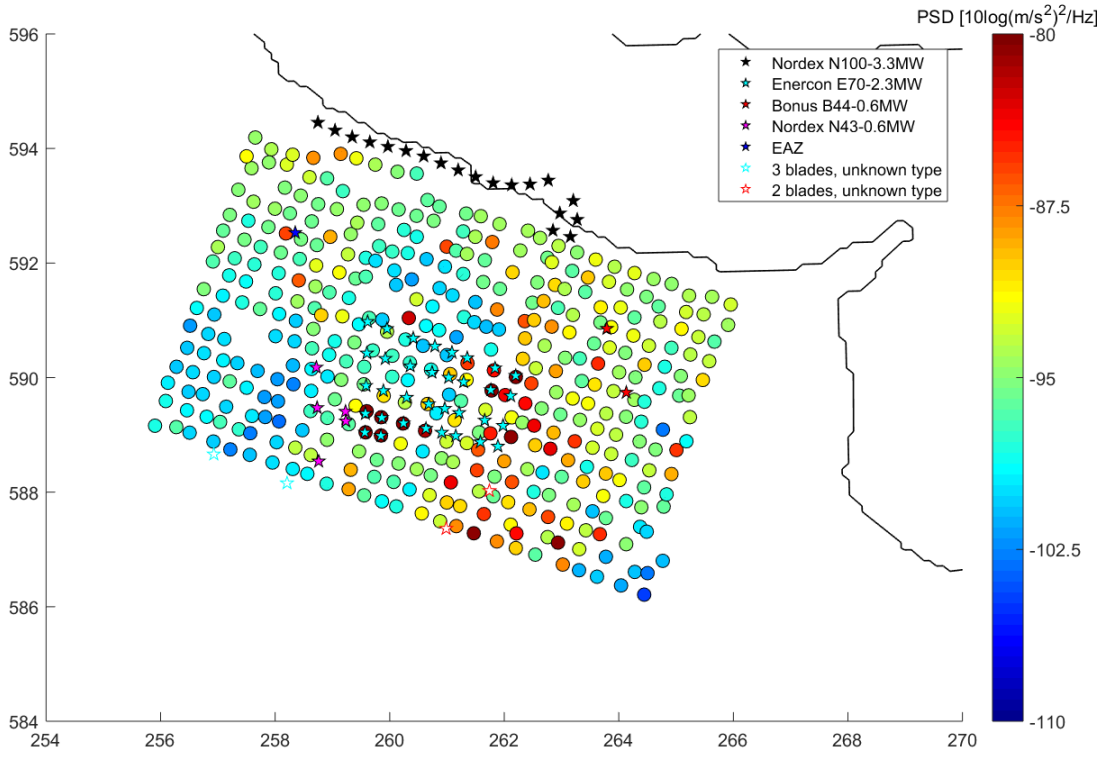


Figure 30: Spatial PSD for the frequency of 0.93 Hz of the N-component during day 11, 2017.

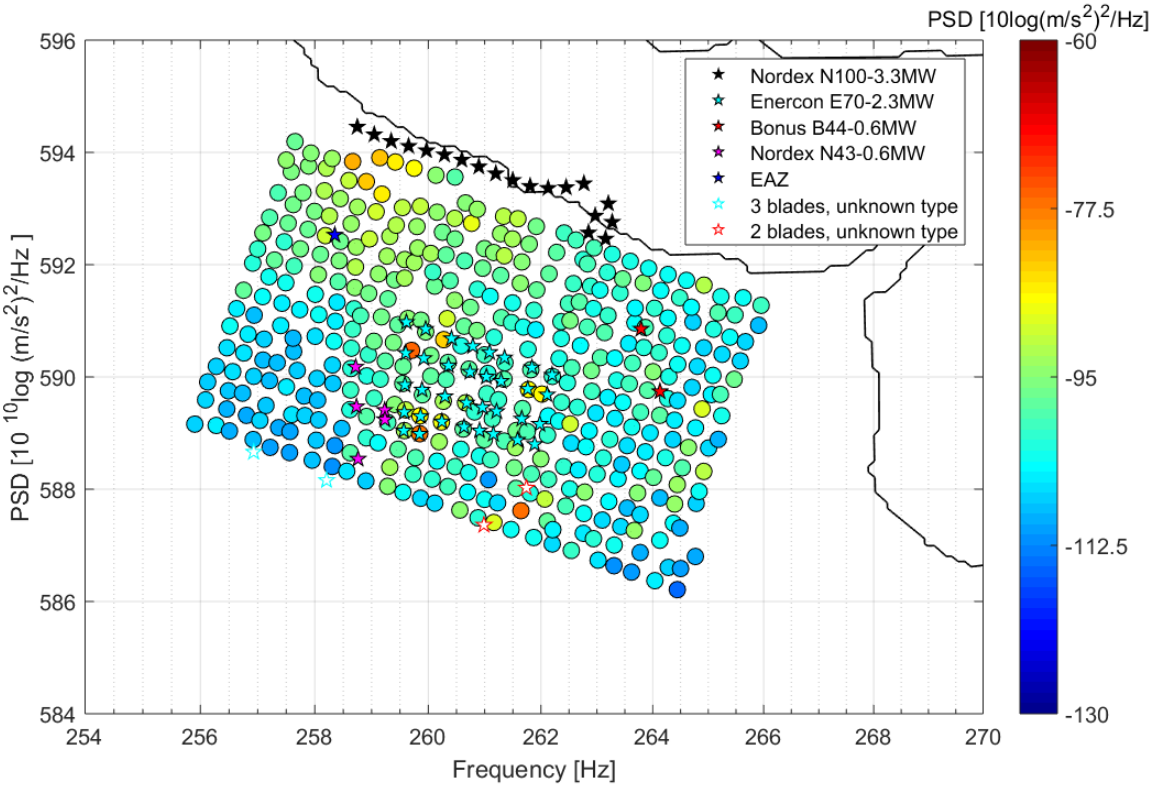


Figure 31: Spatial PSD for the frequency of 0.63 Hz of the Z-component during day 16, 2017.

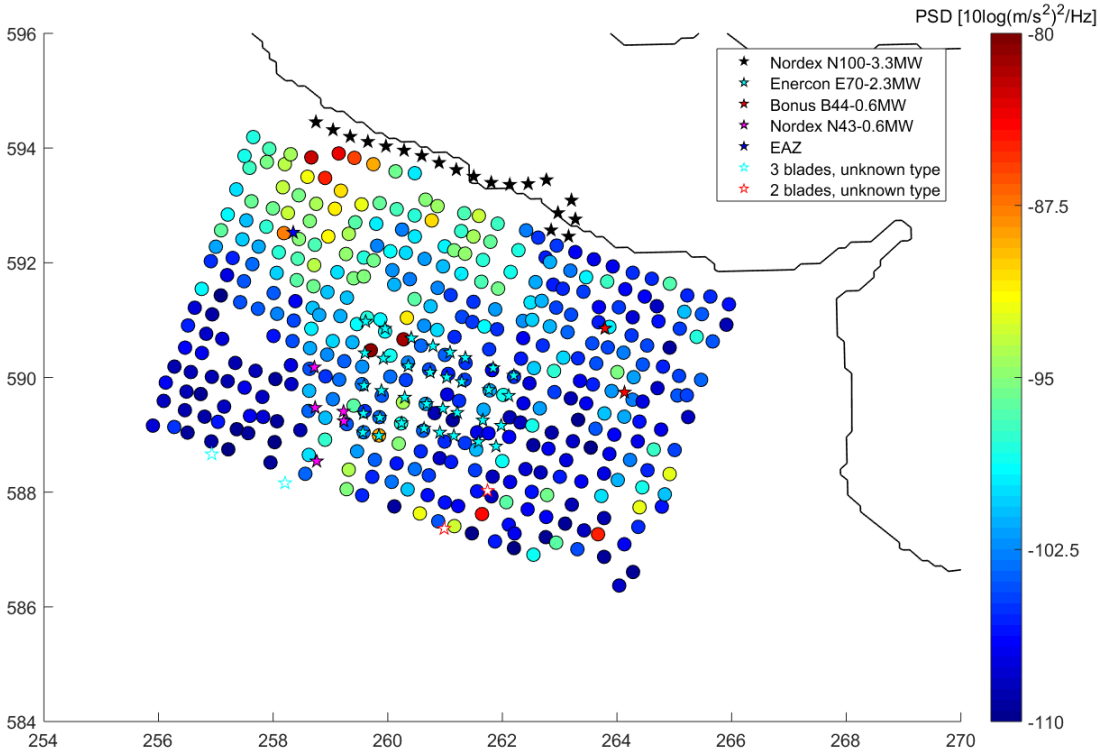


Figure 32: Spatial PSD for the frequency of 1.89 Hz of the Z-component during day 16, 2017.

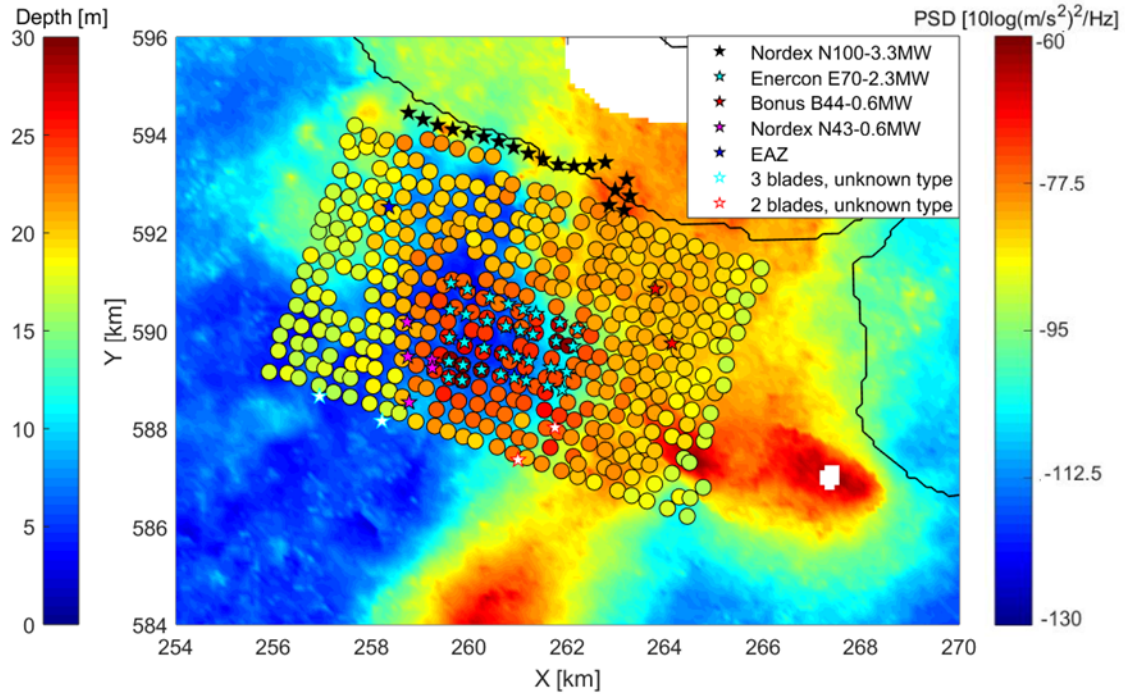


Figure 33: Spatial PSD for the frequency of 2.1 Hz of the Z-component during day 11, 2017, plotted over the depth of the top of the Peelo formation.

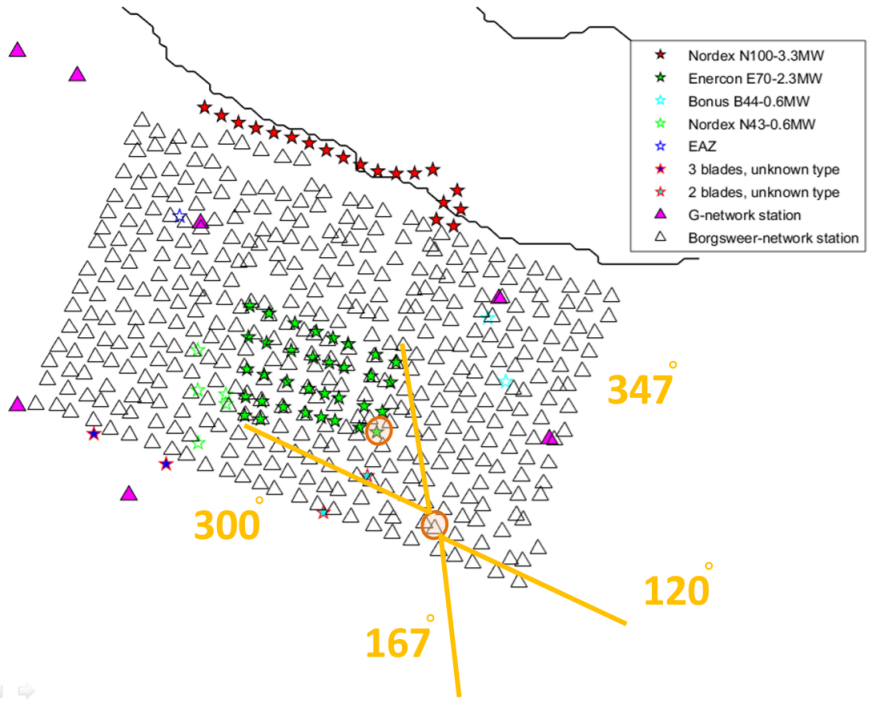


Figure 34: Indication of the chosen WT and station to determine the radiation pattern of the WT as a function of wind direction. Between the indicated angles of 120-167 and 300-347 degrees, the Rayleigh component should dominate according to the theory in section 2.1.

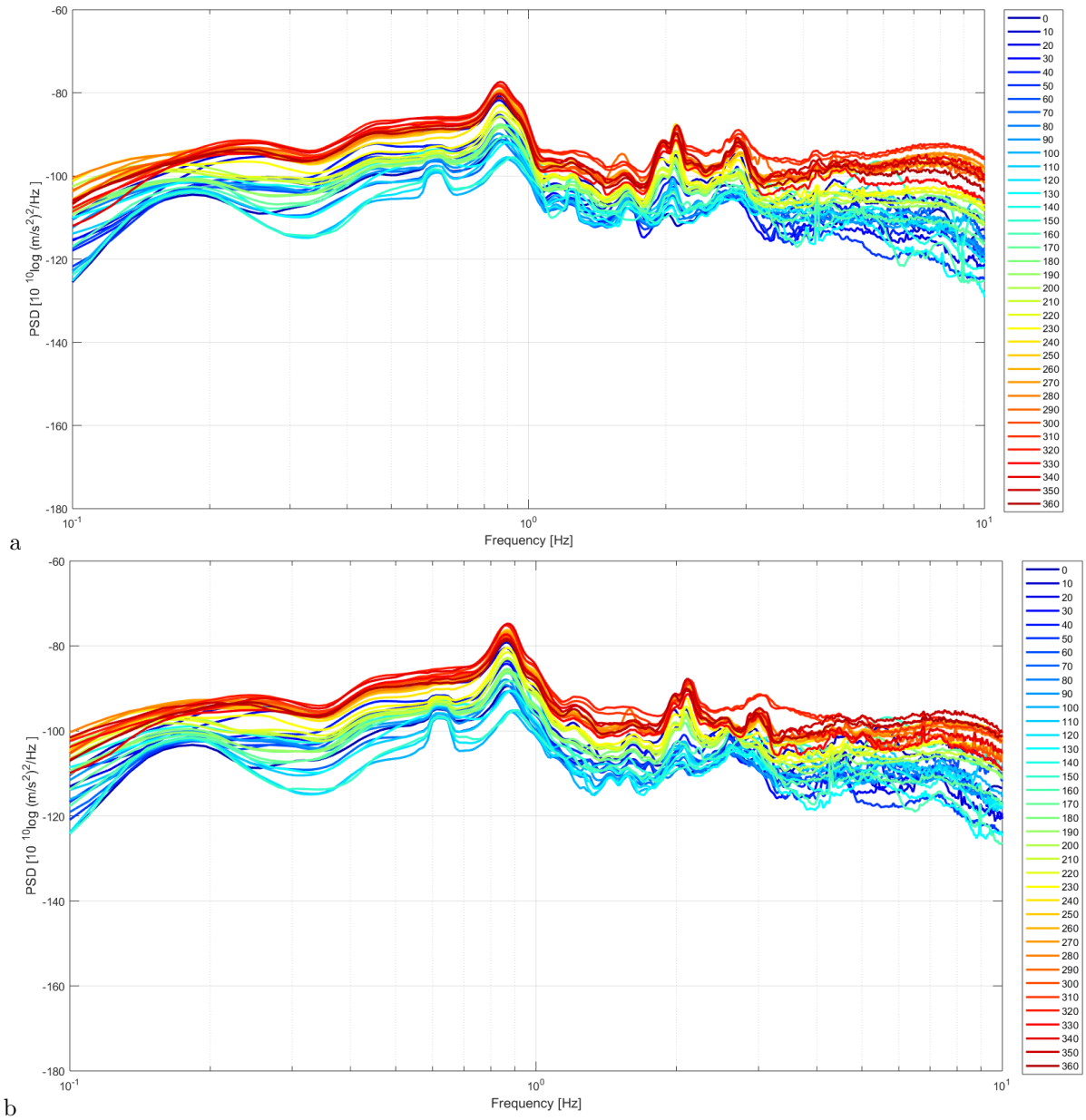


Figure 35: PSD of day 356-366, 2016, and day 2-22, 2017, for a) the radial component and b) the transverse component of station 101.22.

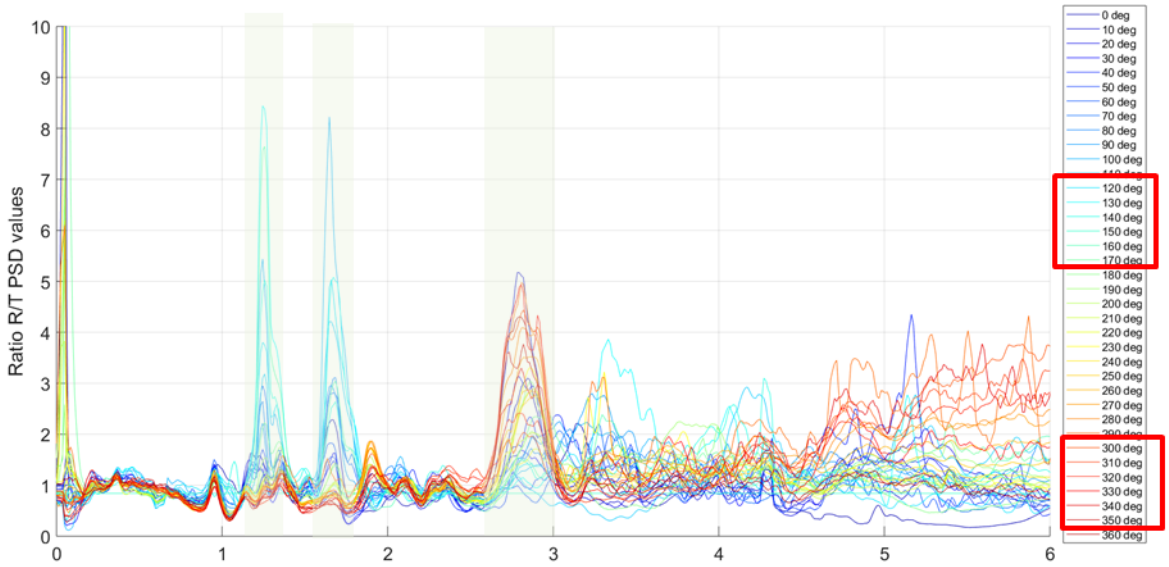


Figure 36: Ratio of the PSDs of day 356-366, 2016, and day 2-22, 2017, for the radial versus the transverse component of station 101.22. The directions that should record a strong Rayleigh (radial) component are indicated in the legend by red boxes. The extreme ratio peaks for these directions are indicated by green bands.

their high ratio: 1.24, 1.89, and 2.79 Hz (Figure 36). These peaks occur at a wind direction of 120-170 degrees (1.24 and 1.89 Hz) and 300-350 degrees (2.8 Hz). These directions are equal to the indicated directions in Figure 34. There is no clear evidence of a R/T ratio lower than 1 at the wind directions perpendicular to those parallel with the WT-station line. No extreme low ratio peaks are recorded between 30-80 and 210-260 degrees wind direction. The wind direction bins are not corrected for wind speed.

## 3.2 Individual WT signal

### 3.2.1 Dispersion curve

Using the method of Park et al. (1998), dispersion curves are constructed for the Borgsweer area in order to define the phase velocity that should be used during beamforming. A possibility to pick multiple maxima per frequency is added so that higher modes can be interpreted. Dispersion curves are made for 1 and 33 days of cross-coherence data input of patch B (Figure 7 for location). The dispersion curve improves with more input data (Figure 37). As input cross-coherence data is used since this gives a higher SNR. Patch B is chosen since for beamforming this patch will be used and therefore it is important to find the phase velocity in that area. A cross-coherence is calculated of the data of all stations in patch B (Figure 38). The causal as well as the acausal results of the cross-coherences are taken into account. Two modes can be distinguished in Figure 37b. It is important to keep in mind that phase velocity always decreases with frequency. In Figure 37b a normal mode and the first overtone are interpreted for frequencies lower than 1 Hz. At higher frequencies these curves do not continue.

### 3.2.2 Beamforming

Jagt (2017) found 2.1 Hz as a strongly WT-related frequency for the Delfzijl South wind park. The spatial PSD in Figure 33 confirms that this frequency is strongly WT-related and most likely usable for beamforming in order to locate individual WTs. Since the dispersion curve did not show a clear mode for frequencies higher than 1 Hz, a range of velocities (0.13-0.32 km/s) is used for beamforming. The

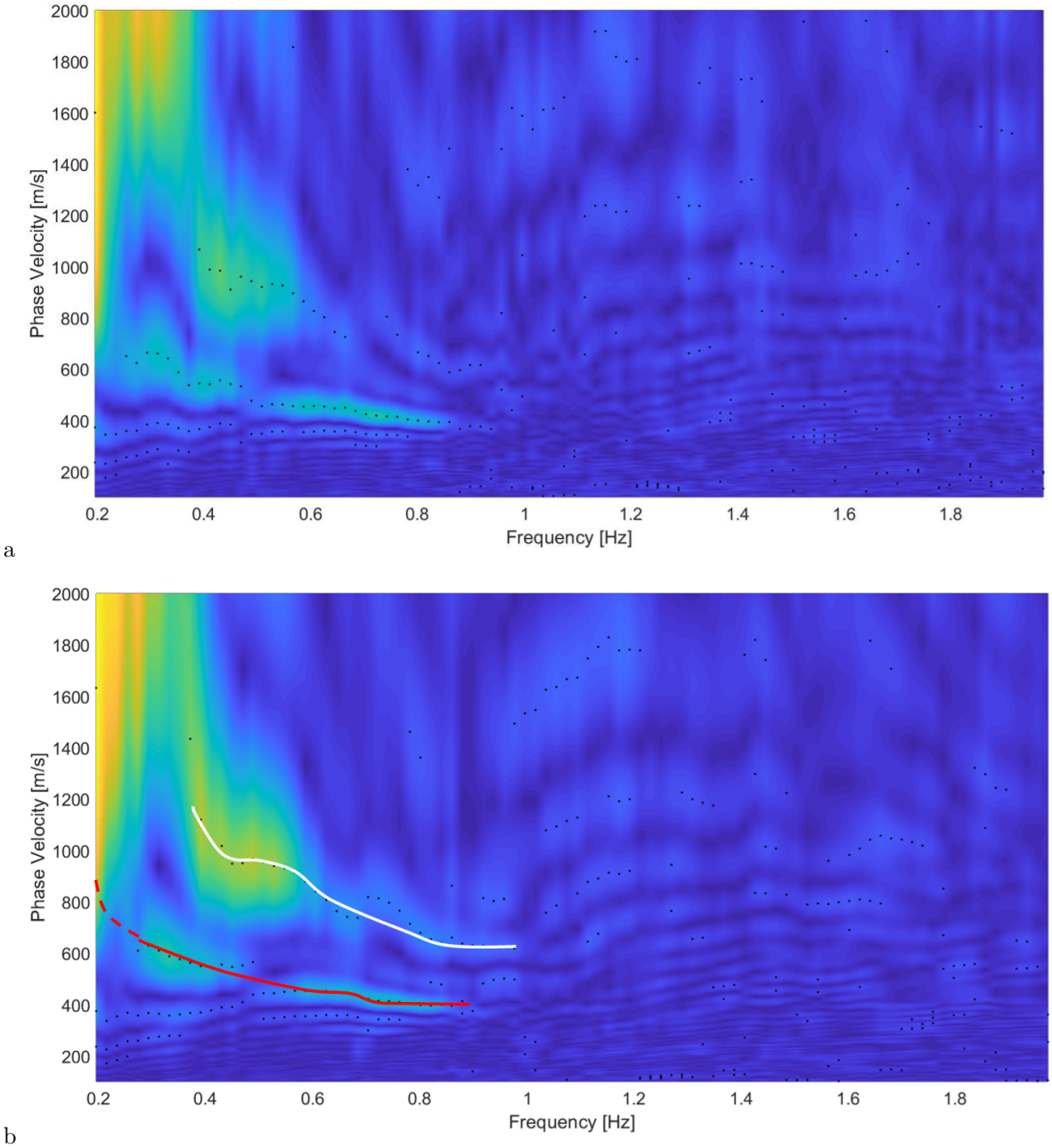


Figure 37: Dispersion curve using the cross-coherences of patch B for a) 1 day of input data, and b)33 days of input data with in red the interpreted fundamental mode and in white the interpreted first higher mode.

beamforming algorithm is applied to one hour of data of patch B (Figure 7), since most WTs of the Delfzijl South wind park are located in this patch. Using the beamforming for the data of all stations is too time-consuming. The goal is to map the beampower and find high power on the locations of the WT. When the power is not located correctly, the inserted velocity can be adjusted. The synthetic test has proven that the error between the inserted velocity and the real velocity cannot be larger than about 8 m/s.

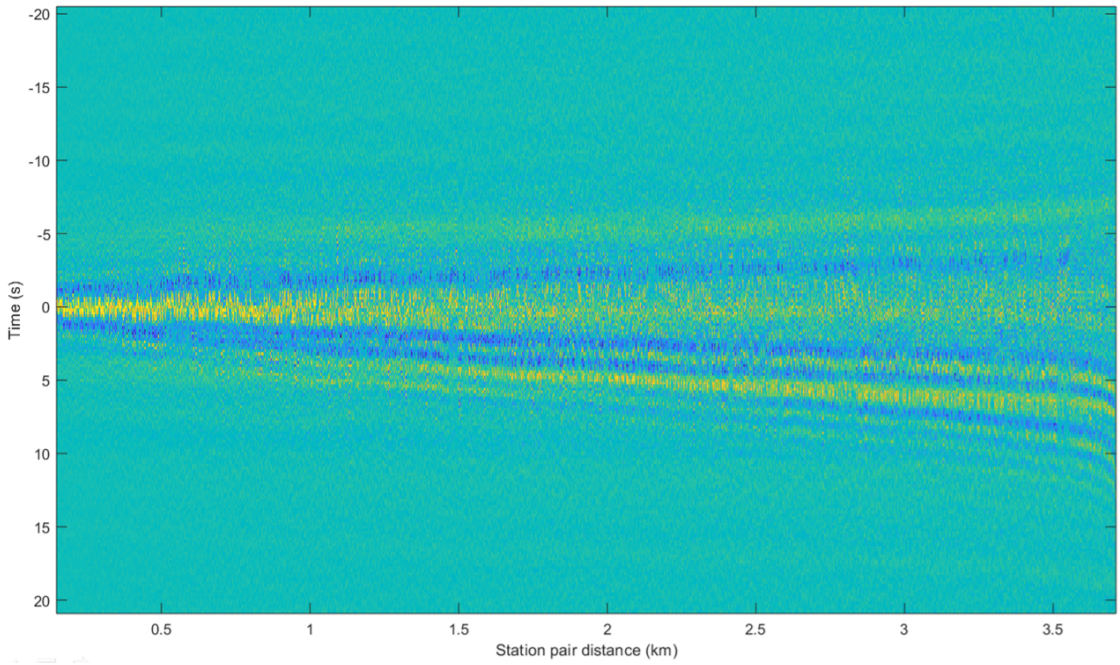


Figure 38: Cross-coherence plot of patch B in the array (see Figure 7).

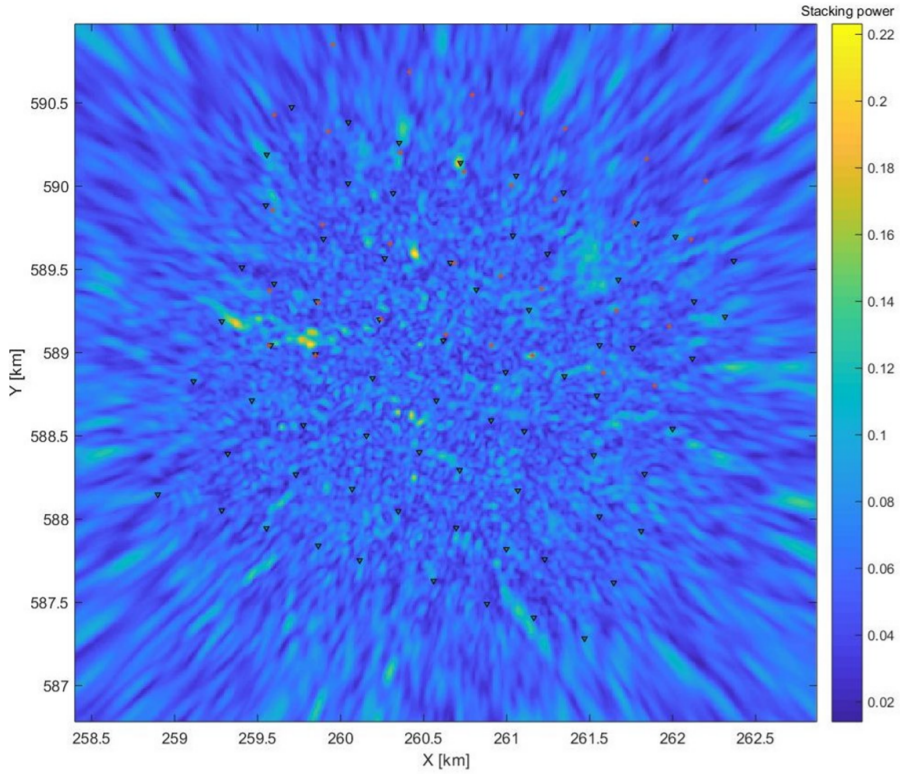


Figure 39: Beamforming result for cross-coherence data of patch B for an inserted velocity of 0.275 km/s. The frequency band is 2.05-2.15 Hz divided over 10 frequency bins. Red dots indicate WT locations, inverted triangles indicate station locations.

The best result of beamforming with real data for the conditions described above is found for an inserted velocity of 0.275 km/s (Figure 39). At some WT locations high powers are found, but not at all locations. In order to be certain that the inserted velocity does not lead to high power at some locations by coincidence, high power should focus in all locations of the WTs in the map. This is not the case in any of the results that are ran for the velocity range 0.13-0.32 km/s.

# 4 Discussion

## 4.1 Local combined WT signal

### 4.1.1 Spectral characteristics

The local combined WT signal can be determined from PSDs. Increasing power with increasing wind speed or decreasing distance to the WT indicates that the frequency at this power is WT-related. It is assumed that the tower of a WT behaves as a clamped beam when moving (Figure 3). Two possible fundamental frequencies of eigenmodes are found in the PSD of a station 15 metres from a WT (Figure 26): 0.31 and 0.63 Hz. Calculating the overtones using the clamped beam theory gives us the following frequency sequences: 0.31, 0.93, 1.55, 2.17, 2.79, 3.41, 4.03, 4.65, 5.27, 5.89, 6.51, 7.13, 7.75, 8.37, 8.99, 9.61, 10.23, 10.85, 11.47 Hz, and 0.63, 1.89, 3.15, 4.41, 5.67, 6.93, 8.19, 9.45, 10.71 Hz. Both in the near-field (Figure 26) and the general PSD (Figure 28) these frequencies show increased power with increasing wind speed, with exception of 3.41, 5.27, 6.51, and 7.75. These frequencies might have been badly represented due to interference of the signal of several WTs in the wind park or due to the heterogeneity of the subsurface.

The hypothesis of two individual fundamental frequencies is in accordance with the data, since the sequences are clearly visible. There are two explanations for finding two different fundamental frequencies: either they are emitted by two different wind parks, or they are emitted by two different movements of the tower. Devriendt et al. (2014) found two different frequencies for the FA and the SS mode of a WT tower, though the difference in frequency was small: 0.361 Hz for the FA mode and 0.366 Hz for the SS mode. The difference between the fundamental frequencies in this study is much larger and therefore it is unlikely that these originate from the FA and SS motion of the WT. From the spatial PSDs in Figure 29 and 30 it seems that the 0.31 and 0.93 Hz frequencies are emitted by the Delfzijl South wind park. The fast decay of the amplitude of the 0.31 Hz frequency is not in accordance with Sato et al. (2012) and Stammler and Ceranna (2016), who stated that higher frequencies attenuate faster than lower frequencies. The reason that the 0.31 Hz frequency attenuates strongly with distance to the WT might be that this frequency is more a tilt movement than an actual propagating wave. The 0.93 Hz frequency is mostly seen at the east of the array. This could be due to the geology as shown for the attenuation of the 2.1 Hz peak in Figure 33. The fact that only 10 WTs in Delfzijl South seem to emit the 0.31 Hz frequency can either be due to the location of the stations or to the fact that there are 10 WTs in the wind park that have slightly different features than the others, as discussed in section 1.3. The 0.31 Hz frequency differs from the 0.39 Hz eigenmode frequency found by Jagt (2017) for the Delfzijl South wind park.

The 0.63 Hz fundamental frequency seems to originate from the Delfzijl North wind park (Figure 31). Both this frequency and its assumed first overtone, 1.89 Hz (Figure 32), have a stronger power in the north of the array, close to the Delfzijl North wind park. It is remarkable that the WTs of the Delfzijl North wind park would have a higher fundamental frequency than the WTs of the Delfzijl South wind park, since the latter are lower (85 versus 100 metres high) and have a smaller power (2.3 versus 3.3 MW) (Appendix). It is though not impossible, since Devriendt et al. (2014) found that the frequency of the eigenmodes is largly dependent on the material of the tower and the foundation. Jagt (2017) found the same eigenmode frequency of 0.63 Hz for the Delfzijl North wind park.

Both PSDs with varying wind speeds (Figures 26 and 28) show a strong power at 2.1 Hz. The maximum of the peak shifts to a higher frequency with increasing wind speed, indicating that the frequency is rotation-related. It is unlikely that the 2.1 Hz frequency is the 1P mode, since 2.1 Hz would mean that a blade makes a complete rotation in approximately 0.48 seconds ($T = 1/f$). This is extremely fast and therefore it is more logically if this frequency is the 3P frequency. There is no peak that could symbolize the 1P around 0.16 Hz. It is likely that the power at this frequency is overpowered by noise.

The frequencies of 1.24, 2.5, 3.28, 3.8, and 5.05 Hz in the PSD for all stations with varying wind speed (Figure 28) show a strong power peak but are not expected to be a multiple of one of the fundamental frequencies. 1.24 and 2.5 Hz show increasing power with wind speed, while 3.28, 3.8 and 5.05 Hz do not. Several large industrial areas are located in Eemshaven and Delfzijl. These might emit noise continuously at the stationary frequencies. The frequencies with an increase of power with an increase of wind speed could be related to interference with other WT waves and resonance of the subsurface (Stammler and Ceranna, 2016).

The 0.87 Hz frequency has a very large power in the recording of the N and E components at station 101.22 (Figure 35). The peak does not show a clear pattern in recordings of other stations or in spatial PSDs. Most likely the peak is not related to the slightly higher frequency of 0.93 Hz (first overtone of 0.31 Hz). If the frequency would be related to the microseism of the ocean, high power would be expected for a much broader frequency band. Most likely the peaking power at the frequency of 0.87 Hz is created by local, non-WT-related influences.

In the description above only the Delfzijl North and Delfzijl South wind park are assumed to be recorded. Obviously the isolated WTs in the area might contribute to the recorded signal, but since their power is so much lower than that of the WTs in the wind parks (maximum 0.6 MW versus at least 2.0 MW) it is more likely that their signal is overpowered by the signal of the WT parks when they interfere with each other. In Figure 33 the individual WTs do not seem to have influence on the recorded power, but rather seem to be overpowered by the radiation pattern of the Delfzijl South wind park.

### 4.1.2 Radiation pattern

The radiation pattern of the WT is studied as a frequency of wind direction. Wind direction does influence the maximum values of the PSD and there the propagating wave is non-radial. This is in accordance with Jagt (2017) and in contrast to Zieger and Ritter (2018). Figure 36 shows the ratio of the radial over the transverse components. The components are decomposed so that the radial component records Rayleigh waves and the transverse component records Love waves. There are two wind directions which should give a high ratio since they are parallel to the line from the WT to the station (Figure 34): 300-350 and 120-170 degrees. This high ratio is indeed shown at the frequencies 1.24, 1.89, and 2.79 Hz in Figure 36. The latter two peaks are first multiples of respectively the eigenmode frequencies 0.63 and 0.31 Hz. This supports the conclusion that both eigenmodes exist. The evidence of emitted Rayleigh waves is strongly supported by the literature in section 1.2.4.

It is harder to distinguish Love waves. These are expected in a range of 30-80 and 210-260 degrees, perpendicular to the wind directions that send a Rayleigh signal to the receiver. It is possible that the emitted Love waves have less power than the emitted Rayleigh waves, since the wind speed in the wind directions that are needed to create Love waves at the receiver are much lower than the wind speeds that send Rayleigh waves to the receiver. To find the directions for a very low R/T ratio (Love wave), it is therefore advisable to correct the wind direction bins for wind speed.

## 4.2 Individual WT signal

### 4.2.1 Dispersion curves

The dispersion curve in Figure 37 is very clear for frequencies under 1 Hz. Two modes can be interpreted: a fundamental mode and the first overtone. Unfortunately a phase velocity could not be established for the frequencies higher than 1 Hz. This could be due to the fact that waves with a higher frequency travel more shallow. From the geological cross section in Figure 9 it is known that the shallow subsurface (to 20 metres depth) is much more heterogeneous than the deeper subsurface (20-50 metres depth). These large dispersive properties could be the reason that the dispersion curves do not continue. Thus, by having used many station combinations in patch B with different velocities, the dispersive properties are in fact averaged out above 1 Hz in Figure 37. The dispersion curve does not contribute to determining a velocity to use for beamforming, since the beamforming will be done for a frequency of 2.1 Hz.

### 4.2.2 Beamforming

From the synthetic test it can be concluded that the CCBF algorithm works well for multiple sources that emit a continuous signal. In the test a homogeneous subsurface is assumed. The velocity error at 2.1 Hz is allowed to be approximately 8 m/s in order to still map the power of the sources at the right locations. From the dispersion curve it can be concluded that the Borgsweer subsurface unfortunately does not resemble a homogeneous subsurface for the depth at which frequencies higher than 1 Hz travel. Thus, the best beamforming result for an inserted velocity of 0.275 km/s does not show the locations of all WTs (Figure 39). Apart from the heterogeneous subsurface, the interference of the seismic signals of multiple WTs in the wind park can play a role. In order to localize all individual WTs, the CCBF algorithm should be rewritten for a varying velocity model, so the heterogeneous subsurface can be taken into account. Possibly the algorithm can work when a smaller array and a smaller number of WTs is studied, since the subsurface will contain less heterogeneity over a smaller surface.

## 4.3 Future studies

When the above suggestions for improvement are applied and the seismic signal of individual WTs is fully characterized, the inversion of subterranean parameters can be studied. It is possible to apply seismic interferometry and look at how useful the measurements are to estimate medium variations. WTs are a good source of seismic signals for using seismic interferometry due to the continuous signal and stable distribution (Jagt, 2017). The term 'seismic interferometry' refers to the principle of generating new seismic responses of virtual sources by cross correlating seismic observations at different receiver locations (Wapenaar et al., 2010). The cross-correlation contains information on the wave velocities of the subsurface between the two receivers. In this case the two receivers would preferably be stationed along a straight line with the WT. When the time delay of the cross-correlation peak and distance between receivers are known, the average velocity between them can be extracted. The time-varying velocities can in theory be used to monitor near-surface properties, such as ground water saturation and ground water level (Jagt, 2017). Furthermore the seismic signal could be used to update velocity and attenuation models.

The characterization of the WT signal that is done in this study can be used to determine the influence of WT generated seismic signals on earthquake monitoring. With a clear idea of the attenuation, spectral characteristics and types of emitted waves it should be possible to correct the earthquake monitoring for the influence of WT seismic signals in the Borgsweer area.

# 5 Conclusion

First, the local combined WT signal is characterized based on attenuation, spectral characteristics, influence of wind speed on the signal, and radiation pattern. The attenuation is found to be strongly dependent on the heterogeneous geology of the area.The signal of the strongly emitted rotation-related frequency of 2.1 Hz does not attenuate completely within the maximum array distance (approximately 3 km).

The spectral characteristics are well defined using the clamped beam theory on the fundamental modes that are found in the near-field of a WT. The conclusion is that the Delfzijl South and North wind park have respectively a fundamental frequency of 0.31 and 0.63 Hz. Most higher modes of these two fundamental frequencies are represented in PSDs with varying wind speed. Higher modes for the frequency of 0.31 Hz are found at 0.93, 1.55, 2.17, 2.79, 3.41, 4.03, 4.65, 5.27, 5.89, 6.51, 7.13, 7.75, 8.37, 8.99, 9.61, 10.23, 10.85, 11.47 Hz. Higher modes for the frequency of 0.63 Hz are found at 1.89, 3.15, 4.41, 5.67, 6.93, 8.19, 9.45, 10.71 Hz. Overtones that are not represented might be lacking power due to interference with other seismic signals. PSDs for varying wind speeds made it possible to distinguish between eigenmode frequencies and rotation-related frequencies. A 3P blade-passing frequency is likely found at 2.1 Hz. The in-explainable peaks in the seismic amplitude spectrum could be due to interference with other WT waves, industrial emitted waves, or resonance of the subsurface.

The WTs radiate surface waves as hypothesized. Parallel to the wind direction a receiver will experience an incoming Rayleigh wave and perpendicular an incoming Love wave for certain frequencies. At other WT related frequency peaks, no clear pattern of the waves can be distinguished. By using varying wind directions, a strongly emitted Rayleigh wave is found for wind directions parallel to the line from the WT to the station. Love waves are more difficult to distinguish. This might be due to the low wind speeds at the wind directions which should induce Love waves.

Secondly, it is tried to characterize the seismic individual WT signal. The synthetic test proved that the CCBF algorithm works for a point source that continuously emits a seismic signal when the subsurface is homogeneous. Unfortunately the established dispersion curve did not continue for frequencies higher than 1 Hz and thus indicated the heterogeneity of the shallow subsurface. Beamforming with the real data for a variety of inserted velocities did not lead to localization of all WTs in the area of subject due to the hetrogeneous subsurface. In future research the algorithm should be altered for a varying velocity model in order to localize all individual WTs.

Even though the localization of the individual WTs could not be completed, we are a large step further at characterizing the seismic signals of WTs. The information on attenuation, spectral characteristics and types of emitted waves can be used to correct the earthquake monitoring for the influence of WT seismic signals in the Borgsweer area.

# 6 Acknowledgements

Many thanks to my supervisor, Elmer Ruigrok, for endless inspiration and effort to help me make this study as successful and complete as possible. I thank my second supervisor, Hanneke Paulssen for the useful feedback that helped me to structure the study as well as possible. Lisanne Jagt, thank you for helping me out with a part of the data processing setup so research could move forward faster and the wheel did not have to be invented twice. I am very grateful for the inspiring time I have had during my research internship at the KNMI.

# 7 References


Adhikari, S. and Bhattacharya, S. (2012). Dynamic analysis of wind turbine towers on flexible foundations. *Shock and vibration*, 19(1):37–56.

Almendros, J., Ibáñez, J. M., Alguacil, G., and Del Pezzo, E. (1999). Array analysis using circular-wave-front geometry: an application to locate the nearby seismo-volcanic source. *Geophysical Journal International*, 136(1):159–170.

Birtill, J. and Whiteway, F. (1965). The application of phased arrays to the analysis of seismic body waves. *Phil. Trans. R. Soc. Lond. A*, 258(1091):421–493.

Devriendt, C., Weijtjens, W., El-Kafafy, M., and De Sitter, G. (2014). Monitoring resonant frequencies and damping values of an offshore wind turbine in parked conditions. *IET Renewable Power Generation*, 8(4):433–441.

Dost, B., Ruigrok, E., and Spetzler, J. (2017). Development of seismicity and probabilistic hazard assessment for the groningen gas field. *Netherlands Journal of Geosciences*, 96(5):s235–s245.

DotX Control Solutions B.V. (2018). Dotx wind turbine controller. `https://www.dotxcontrol.com/wind-turbine-control` (Accessed 19-09-2018).

Eneco (2017). Wat is windenergie? `https://blog.eneco.be/groen/wat-is-windenergie/`, (Accessed 06-03-2019).

Estrella, H. F., Korn, M., and Alberts, K. (2017). Analysis of the influence of wind turbine noise on seismic recordings at two wind parks in germany. *Journal of Geoscience and Environment Protection*, 5(05):76.

Friedrich, T., Zieger, T., Forbriger, T., and Ritter, J. R. (2018). Locating wind farms by seismic interferometry and migration. *Journal of Seismology*, pages 1–15.

Gortsas, T. V., Triantafyllidis, T., Chrisopoulos, S., and Polyzos, D. (2017). Numerical modelling of micro-seismic and infrasound noise radiated by a wind turbine. *Soil Dynamics and Earthquake Engineering*, 99:108–123.

Grotzinger, J., Jordan, T. H., and Press, F. (2010). *Understanding earth*. Macmillan.

Jagt, L. (2017). Characterizing seismic signals from wind farms in groningen. *Guided reseach, Utrecht University*.

Kruiver, P. P., van Dedem, E., Romijn, R., de Lange, G., Korff, M., Stafleu, J., Gunnink, J. L., Rodriguez-Marek, A., Bommer, J. J., van Elk, J., et al. (2017). An integrated shear-wave velocity model for the groningen gas field, the netherlands. *Bulletin of Earthquake Engineering*, 15(9):3555–3580.

McMechan, G. A. and Yedlin, M. J. (1981). Analysis of dispersive waves by wave field transformation. *Geophysics*, 46(6):869–874.

McNamara, D. E. and Buland, R. P. (2004). Ambient noise levels in the continental united states. *Bulletin of the seismological society of America*, 94(4):1517–1527.

Neuffer, T. and Kremers, S. (2017). How wind turbines affect the performance of seismic monitoring stations and networks. *Geophysical Journal International*, 211(3):1319–1327.

NOAA (2018). Noaa solar calculator. `https://www.esrl.noaa.gov/gmd/grad/solcalc/` (Accessed 24-09-2018).

Noorlandt, R., Kruiver, P. P., de Kleine, M. P., Karaoulis, M., de Lange, G., Di Matteo, A., von Ketelhodt, J., Ruigrok, E., Edwards, B., Rodriguez-Marek, A., et al. (2018). Characterisation of ground motion recording stations in the groningen gas field. *Journal of seismology*, 22(3):605–623.

Park, C. B., Miller, R. D., and Xia, J. (1998). Imaging dispersion curves of surface waves on multi-channel record. In *SEG Technical Program Expanded Abstracts 1998*, pages 1377–1380. Society of Exploration Geophysicists, Further information can be found at `http://www.masw.com/DCImagingScheme.html`.

Peterson, J. et al. (1993). Observations and modeling of seismic background noise.

Pigge, M. (2017). Bestemmingsplan "windpark delfzijl zuid uitbreiding" toelichting. *Gemeente Delfzijl*.

Ruigrok, E., Gibbons, S., and Wapenaar, K. (2017). Cross-correlation beamforming. *Journal of Seismology*, 21(3):495–508.

Saccorotti, G., Piccinini, D., Cauchie, L., and Fiori, I. (2011). Seismic noise by wind farms: a case study from the virgo gravitational wave observatory, italy. *Bulletin of the Seismological Society of America*, 101(2):568–578.

Sato, H., Fehler, M. C., and Maeda, T. (2012). *Seismic wave propagation and scattering in the heterogeneous earth*, volume 496. Springer.

Schofield, R. (2001). *Seismic measurements at the stateline wind project*. Rept No LIGO T020104-00-/, Laser Interferometer Gravitational Wave Observatory available at `http://www.ligo.caltech.edu/docs`.

Schweitzer, J., Fyen, J., Mykkeltveit, S., Kværna, T., and Bormann, P. (2002). Seismic arrays. *IASPEI new manual of seismological observatory practice*, pages 31–32.

Stafleu, J., Maljers, D., Busschers, F., Gunnink, J., Schokker, J., Dambrink, R., Hummelman, H., and Schijf, M. (2012). Geotop modellering. *TNO report*, 10991.

Stafleu, J., Maljers, D., Gunnink, J., Menkovic, A., and Busschers, F. (2011). 3d modelling of the shallow subsurface of zeeland, the netherlands. *Netherlands Journal of Geosciences*, 90(4):293–310.

Stammler, K. and Ceranna, L. (2016). Influence of wind turbines on seismic records of the gräfenberg array. *Seismological Research Letters*, 87(5):1075–1081.

Styles, P., England, R., Stimpson, I. G., Toon, S., Bowers, D., and Hayes, M. (2005). A detailed study of the propagation and modelling of the eects of low frequency seismic vibration and infrasound from wind turbines. (pp. 17-18). First International Meeting on Wind Turbine Noise: Perspectives for Control: Berlin.

TNO (2013). Lithostratigrafische nomenclator van de ondiepe ondergrond, versie 2013. Retrieved 14-02-2019 from `https://www.dinoloket.nl/nomenclator-ondiep`.

TNO (2016). Dinoloket: Data en informatie van de nederlandse ondergrond. Retrieved 19-02-2019 from `https://www.dinoloket.nl/ondergrondmodellen`.

Van der Tempel, J. and Molenaar, D.-P. (2002). Wind turbine structural dynamics–a review of the principles for modern power generation, onshore and offshore. *Wind engineering*, 26(4):211–222.

Wapenaar, K., Draganov, D., Snieder, R., Campman, X., and Verdel, A. (2010). Tutorial on seismic interferometry: Part 1—basic principles and applications. *Geophysics*, 75(5):75A195–75A209.

Westwood, R. F. and Styles, P. (2017). Assessing the seismic wavefield of a wind turbine using polarization analysis. *Wind Energy*, 20(11):1841–1850.

Westwood, R. F., Styles, P., and Toon, S. M. (2015). Seismic monitoring and vibrational characterization of small wind turbines: A case study of the potential effects on the eskdalemuir international monitoring system station in scotland. *Near Surface Geophysics*, 13(2):115–126.

Xi Engineering Consultants Ltd (2014). Seismic vibration produced by wind turbines in the eskdalemuir region. Available on `https://www.gov.scot/Topics/Business-Industry/Energy/Infrastructure/Energy-Consents/Guidance/reportseismicvibrations`.

Zieger, T. and Ritter, J. R. (2018). Influence of wind turbines on seismic stations in the upper rhine graben, sw germany. *Journal of Seismology*, 22(1):105–122.

# 8 Appendix

locatieswt

| Wind farm | Type | X_RD | Y_RD | Degrees E | Degrees N | Hub height (m) | Rotor diameter (m) | ID |
|---|---|---|---|---|---|---|---|---|
| Eemshaven | Lagerwey L136-4.5MW | 248.339212 | 607.816696 | 6.792098 | 53.448382 | 132 | 136 | 4 |
| Eemshaven | Lagerwey L136-4.5MW | 249.631811 | 607.785892 | 6.811539 | 53.447877 | 132 | 136 | 10 |
| Eemshaven | Repower 6.15MW | 250.215607 | 607.768794 | 6.820318 | 53.447619 | 114 | 126 | 219 |
| Eemshaven | Repower 6.15MW | 250.737381 | 607.639706 | 6.82813 | 53.446366 | 114 | 126 | 225 |
| Eemshaven | 2-B Energy-6MW | 248.89897 | 608.57725 | 6.800746 | 53.455115 | 105 | 70 | 191 |
| Eemshaven | Enercon E82-3.0 MW | 245.293294 | 609.055424 | 6.746618 | 53.460035 | 100 | 82 | 94 |
| Eemshaven | Enercon E82-3.0 MW | 245.5908 | 609.022364 | 6.751087 | 53.459688 | 100 | 82 | 93 |
| Eemshaven | Enercon E82-3.0 MW | 245.885859 | 608.975513 | 6.755514 | 53.459216 | 100 | 82 | 92 |
| Eemshaven | Enercon E82-3.0 MW | 246.171618 | 608.887609 | 6.75979 | 53.458378 | 100 | 82 | 91 |
| Eemshaven | Enercon E82-3.0 MW | 246.446932 | 608.80535 | 6.76391 | 53.457592 | 100 | 82 | 90 |
| Eemshaven | Enercon E82-3.0 MW | 246.748083 | 608.713002 | 6.768416 | 53.45671 | 100 | 82 | 89 |
| Eemshaven | Enercon E82-3.0 MW | 247.033735 | 608.624785 | 6.772689 | 53.455868 | 100 | 82 | 85 |
| Eemshaven | Enercon E82-3.0 MW | 247.310567 | 608.499971 | 6.776819 | 53.454699 | 100 | 82 | 84 |
| Eemshaven | Enercon E82-3.0 MW | 247.592865 | 608.379051 | 6.781032 | 53.453564 | 100 | 82 | 83 |
| Eemshaven | Enercon E82-3.0 MW | 247.866213 | 608.254617 | 6.785109 | 53.452399 | 100 | 82 | 82 |
| Eemshaven | Enercon E82-3.0 MW | 248.142009 | 608.103394 | 6.789215 | 53.450992 | 100 | 82 | 5 |
| Eemshaven | Enercon E82-3.0 MW | 246.04634 | 608.350601 | 6.75775 | 53.453576 | 100 | 82 | 86 |
| Eemshaven | Enercon E82-3.0 MW | 246.336117 | 608.278779 | 6.76209 | 53.452881 | 100 | 82 | 87 |
| Eemshaven | Enercon E82-3.0 MW | 246.621247 | 608.186016 | 6.766355 | 53.451998 | 100 | 82 | 198 |
| Eemshaven | Enercon E82-3.0 MW | 246.906981 | 608.088629 | 6.770626 | 53.451074 | 100 | 82 | 3 |
| Eemshaven | Enercon E82-3.0 MW | 247.18256 | 607.980461 | 6.774742 | 53.450055 | 100 | 82 | 200 |
| Eemshaven | Enercon E82-3.0 MW | 247.469233 | 607.871113 | 6.779024 | 53.449023 | 100 | 82 | 2 |
| Eemshaven | Enercon E82-3.0 MW | 248.125876 | 607.372296 | 6.788758 | 53.444428 | 100 | 82 | 98 |
| Eemshaven | Enercon E82-3.0 MW | 248.443703 | 607.404637 | 6.793549 | 53.444662 | 100 | 82 | 12 |
| Eemshaven | Enercon E82-3.0 MW | 248.839582 | 607.403219 | 6.799505 | 53.44458 | 100 | 82 | 13 |
| Eemshaven | Enercon E82-3.0 MW | 249.20629 | 607.346198 | 6.805006 | 53.444003 | 100 | 82 | 97 |
| Eemshaven | Enercon E82-3.0 MW | 249.509835 | 607.296933 | 6.809558 | 53.443507 | 100 | 82 | 80 |
| Eemshaven | Enercon E82-3.0 MW | 249.862321 | 607.249034 | 6.814847 | 53.443014 | 100 | 82 | 81 |
| Eemshaven | Enercon E82-3.0 MW | 250.210935 | 607.19961 | 6.820077 | 53.442507 | 100 | 82 | 73 |
| Eemshaven | Enercon E82-3.0 MW | 250.562344 | 607.131639 | 6.825344 | 53.441834 | 100 | 82 | 183 |
| Eemshaven | Enercon E82-3.0 MW | 250.919939 | 607.046485 | 6.830698 | 53.441004 | 100 | 82 | 74 |
| Eemshaven | Enercon E82-3.0 MW | 251.274892 | 606.958209 | 6.836011 | 53.440147 | 100 | 82 | 75 |
| Eemshaven | Enercon E82-3.0 MW | 251.605323 | 606.879303 | 6.840958 | 53.439379 | 100 | 82 | 76 |
| Eemshaven | Enercon E82-3.0 MW | 251.933528 | 606.801215 | 6.845872 | 53.438622 | 100 | 82 | 77 |
| Eemshaven | Enercon E82-3.0 MW | 252.263303 | 606.724912 | 6.850809 | 53.437872 | 100 | 82 | 78 |
| Eemshaven | Enercon E82-3.0 MW | 252.576669 | 606.566039 | 6.855474 | 53.436387 | 100 | 82 | 79 |
| Eemshaven | Enercon E82-3.0 MW | 252.88107 | 606.382817 | 6.859997 | 53.434686 | 100 | 82 | 203 |
| Eemshaven | Enercon E82-3.0 MW | 253.173536 | 606.21009 | 6.864343 | 53.43308 | 100 | 82 | 197 |
| Eemshaven | Enercon E82-3.0 MW | 253.353538 | 605.929375 | 6.866813 | 53.430527 | 100 | 82 | 114 |
| Eemshaven | Enercon E82-3.0 MW | 253.489908 | 605.644554 | 6.868926 | 53.427942 | 100 | 82 | 105 |
| Eemshaven | Enercon E82-3.0 MW | 253.635328 | 605.359938 | 6.871025 | 53.425359 | 100 | 82 | 201 |
| Eemshaven | Enercon E82-3.0 MW | 253.830102 | 604.979958 | 6.873836 | 53.421909 | 100 | 82 | 139 |
| Eemshaven | Enercon E82-3.0 MW | 253.996134 | 605.472879 | 6.876486 | 53.426306 | 100 | 82 | 106 |
| Eemshaven | Enercon E82-3.0 MW | 253.756682 | 606.065982 | 6.873069 | 53.431678 | 100 | 82 | 14 |
| Eemshaven | Enercon E82-3.0 MW | 253.843487 | 606.41492 | 6.874483 | 53.434796 | 100 | 82 | 15 |
| Eemshaven | Enercon E82-3.0 MW | 254.150244 | 605.98462 | 6.878963 | 53.430874 | 100 | 82 | 16 |
| Eemshaven | Enercon E82-3.0 MW | 253.549485 | 606.472824 | 6.870079 | 53.435372 | 100 | 82 | 21 |
| Eemshaven | Enercon E82-3.0 MW | 253.416246 | 607.202802 | 6.868301 | 53.441952 | 100 | 82 | 19 |

| | | | | | | | | |
|---|---|---|---|---|---|---|---|---|
| Eemshaven | Enercon E82-3.0 MW | 253.301621 | 606.731565 | 6.866431 | 53.437741 | 100 | 82 | 20 |
| Eemshaven | Enercon E82-3.0 MW | 253.660191 | 606.942201 | 6.87189 | 53.439566 | 100 | 82 | 17 |
| Eemshaven | Enercon E82-3.0 MW | 254.271525 | 606.916729 | 6.881079 | 53.439224 | 100 | 82 | 24 |
| Eemshaven | Enercon E82-3.0 MW | 253.953122 | 606.875581 | 6.876276 | 53.438914 | 100 | 82 | 25 |
| Eemshaven | Enercon E82-3.0 MW | 254.02562 | 607.171451 | 6.877459 | 53.441558 | 100 | 82 | 193 |
| Eemshaven | Enercon E82-3.0 MW | 253.756202 | 607.439889 | 6.873489 | 53.444019 | 100 | 82 | 192 |
| Eemshaven | Enercon E82-3.0 MW | 253.548505 | 607.638769 | 6.870426 | 53.445844 | 100 | 82 | 18 |
| Eemshaven | Enercon E82-3.0 MW | 253.250681 | 607.911275 | 6.866029 | 53.448347 | 100 | 82 | 194 |
| Eemshaven | Enercon E82-3.0 MW | 252.95111 | 608.13192 | 6.86159 | 53.450384 | 100 | 82 | 35 |
| Eemshaven | Enercon E82-3.0 MW | 252.642563 | 608.295465 | 6.856997 | 53.45191 | 100 | 82 | 34 |
| Eemshaven | Enercon E82-3.0 MW | 251.690961 | 608.611375 | 6.842774 | 53.454921 | 100 | 82 | 33 |
| Eemshaven | Enercon E82-3.0 MW | 250.997064 | 608.934394 | 6.832429 | 53.457949 | 100 | 82 | 9 |
| Eemshaven | Enercon E82-3.0 MW | 250.664249 | 609.060974 | 6.827458 | 53.459146 | 100 | 82 | 29 |
| Eemshaven | Enercon E82-3.0 MW | 250.334729 | 609.194618 | 6.822539 | 53.460405 | 100 | 82 | 188 |
| Eemshaven | Enercon E82-3.0 MW | 250.004699 | 609.322652 | 6.81761 | 53.461614 | 100 | 82 | 26 |
| Eemshaven | Enercon E82-3.0 MW | 249.671099 | 609.31449 | 6.812586 | 53.461601 | 100 | 82 | 23 |
| Eemshaven | Enercon E82-3.0 MW | 249.24058 | 608.901315 | 6.805983 | 53.457966 | 100 | 82 | 22 |
| Eemshaven | Enercon E82-3.0 MW | 248.607399 | 608.254227 | 6.796263 | 53.452265 | 100 | 82 | 199 |
| Eemshaven | Enercon E82-3.0 MW | 249.023062 | 608.153955 | 6.802488 | 53.451291 | 100 | 82 | 212 |
| Eemshaven | Enercon E82-3.0 MW | 249.411759 | 608.05178 | 6.808307 | 53.450304 | 100 | 82 | 8 |
| Eemshaven | Enercon E82-3.0 MW | 246.748083 | 608.713002 | 6.768416 | 53.45671 | 100 | 82 | 88 |
| Eemshaven | Enercon E82-3.0 MW | 252.325151 | 608.422586 | 6.85226 | 53.45311 | 100 | 82 | 40 |
| Eemshaven | Vestas V90-3.0MW | 252.006629 | 608.545461 | 6.847514 | 53.45428 | 100 | 90 | 247 |
| Eemshaven | Vestas V90-3.0MW | 245.463996 | 608.499805 | 6.749029 | 53.455015 | 100 | 90 | 108 |
| Eemshaven | Vestas V90-3.0MW | 245.779436 | 608.421546 | 6.753754 | 53.454258 | 100 | 90 | 110 |
| Eemshaven | Vestas V90-3.0MW | 248.736937 | 607.790444 | 6.798075 | 53.448076 | 100 | 90 | 1 |
| Eemshaven | Vestas V90-3.0MW | 249.552997 | 608.82711 | 6.810663 | 53.457244 | 100 | 90 | 184 |
| Eemshaven | Vestas V90-3.0MW | 249.86589 | 608.751907 | 6.81535 | 53.456512 | 100 | 90 | 185 |
| Eemshaven | Vestas V90-3.0MW | 250.209871 | 608.66784 | 6.820502 | 53.455696 | 100 | 90 | 151 |
| Eemshaven | Vestas V90-3.0MW | 250.549921 | 608.585097 | 6.825594 | 53.454892 | 100 | 90 | 152 |
| Eemshaven | Vestas V90-3.0MW | 250.892 | 608.503 | 6.830717 | 53.454093 | 100 | 90 | 41 |
| Eemshaven | Vestas V90-3.0MW | 251.347102 | 607.248618 | 6.837185 | 53.442743 | 100 | 90 | 156 |
| Eemshaven | Vestas V90-3.0MW | 251.676757 | 607.185047 | 6.842126 | 53.442112 | 100 | 90 | 153 |
| Eemshaven | Vestas V90-3.0MW | 252.007049 | 607.106636 | 6.847071 | 53.441348 | 100 | 90 | 154 |
| Eemshaven | Vestas V90-3.0MW | 252.339137 | 607.033706 | 6.852044 | 53.440632 | 100 | 90 | 158 |
| Eemshaven | Vestas V90-3.0MW | 252.652696 | 606.888752 | 6.856717 | 53.439272 | 100 | 90 | 159 |
| Eemshaven | Vestas V90-3.0MW | 252.955796 | 606.706214 | 6.86122 | 53.437577 | 100 | 90 | 160 |
| Eemshaven | Vestas V90-3.0MW | 252.853246 | 607.714582 | 6.859989 | 53.446653 | 100 | 90 | 157 |
| Eemshaven | Vestas V90-3.0MW | 252.143076 | 607.674697 | 6.849291 | 53.446425 | 100 | 90 | 36 |
| Eemshaven | Vestas V90-3.0MW | 252.219827 | 607.985844 | 6.850541 | 53.449206 | 100 | 90 | 37 |
| Eemshaven | Vestas V90-3.0MW | 251.791745 | 607.666761 | 6.844002 | 53.446418 | 100 | 90 | 38 |
| Eemshaven | Vestas V90-3.0MW | 245.16 | 608.565 | 6.74447 | 53.45564 | 100 | 90 | 248 |
| Eemshaven | Vestas V90-3.0MW | 251.564708 | 608.174524 | 6.840741 | 53.45102 | 100 | 90 | 39 |
| Delfzijl Noord | Nordex N100-3.3MW | 258.747559 | 594.455208 | 6.944353 | 53.326436 | 100 | 100 | 228 |
| Delfzijl Noord | Nordex N100-3.3MW | 259.045988 | 594.318283 | 6.948786 | 53.325148 | 100 | 100 | 229 |
| Delfzijl Noord | Nordex N100-3.3MW | 259.345545 | 594.200771 | 6.953242 | 53.324034 | 100 | 100 | 230 |
| Delfzijl Noord | Nordex N100-3.3MW | 259.653385 | 594.110622 | 6.957831 | 53.323183 | 100 | 100 | 231 |
| Delfzijl Noord | Nordex N100-3.3MW | 259.969273 | 594.034028 | 6.962545 | 53.322414 | 100 | 100 | 232 |
| Delfzijl Noord | Nordex N100-3.3MW | 260.286369 | 593.960597 | 6.967278 | 53.321692 | 100 | 100 | 233 |

| | | | | | | | | |
|---|---|---|---|---|---|---|---|---|
| Delfzijl Noord | Nordex N100-3.3MW | 260.595069 | 593.866296 | 6.971878 | 53.320784 | 100 | 100 | 234 |
| Delfzijl Noord | Nordex N100-3.3MW | 260.896762 | 593.74581 | 6.976364 | 53.319642 | 100 | 100 | 235 |
| Delfzijl Noord | Nordex N100-3.3MW | 261.197252 | 593.6232 | 6.980831 | 53.318481 | 100 | 100 | 236 |
| Delfzijl Noord | Nordex N100-3.3MW | 261.499992 | 593.505 | 6.985333 | 53.317359 | 100 | 100 | 237 |
| Delfzijl Noord | Nordex N100-3.3MW | 261.806812 | 593.398933 | 6.9899 | 53.316345 | 100 | 100 | 238 |
| Delfzijl Noord | Nordex N100-3.3MW | 262.128942 | 593.363141 | 6.99472 | 53.315959 | 100 | 100 | 239 |
| Delfzijl Noord | Nordex N100-3.3MW | 262.450622 | 593.377458 | 6.999549 | 53.316023 | 100 | 100 | 240 |
| Delfzijl Noord | Nordex N100-3.3MW | 262.769115 | 593.444494 | 7.004349 | 53.316561 | 100 | 100 | 241 |
| Delfzijl Noord | Nordex N100-3.3MW | 262.850139 | 592.569048 | 7.005269 | 53.308681 | 100 | 100 | 242 |
| Delfzijl Noord | Nordex N100-3.3MW | 262.970781 | 592.87012 | 7.00718 | 53.311361 | 100 | 100 | 243 |
| Delfzijl Noord | Nordex N100-3.3MW | 263.205872 | 593.088831 | 7.01078 | 53.313278 | 100 | 100 | 244 |
| Delfzijl Noord | Nordex N100-3.3MW | 263.274395 | 592.758841 | 7.011696 | 53.3103 | 100 | 100 | 245 |
| Delfzijl Noord | Nordex N100-3.3MW | 263.155572 | 592.460585 | 7.009813 | 53.307645 | 100 | 100 | 246 |
| Delfzijl Zuid | Enercon E70-2.3MW | 259.615232 | 590.975971 | 6.956233 | 53.295015 | 85 | 71 | 149 |
| Delfzijl Zuid | Enercon E70-2.3MW | 259.95399 | 590.852952 | 6.961272 | 53.293843 | 85 | 71 | 215 |
| Delfzijl Zuid | Enercon E70-2.3MW | 260.412018 | 590.68567 | 6.968084 | 53.292251 | 85 | 71 | 162 |
| Delfzijl Zuid | Enercon E70-2.3MW | 260.790106 | 590.54828 | 6.973706 | 53.290942 | 85 | 71 | 163 |
| Delfzijl Zuid | Enercon E70-2.3MW | 261.086934 | 590.439577 | 6.97812 | 53.289906 | 85 | 71 | 164 |
| Delfzijl Zuid | Enercon E70-2.3MW | 261.353473 | 590.343575 | 6.982084 | 53.288991 | 85 | 71 | 165 |
| Delfzijl Zuid | Enercon E70-2.3MW | 261.840758 | 590.165225 | 6.989329 | 53.287292 | 85 | 71 | 216 |
| Delfzijl Zuid | Enercon E70-2.3MW | 262.200498 | 590.034682 | 6.994678 | 53.286047 | 85 | 71 | 170 |
| Delfzijl Zuid | Enercon E70-2.3MW | 259.601912 | 590.426145 | 6.955854 | 53.290079 | 85 | 71 | 125 |
| Delfzijl Zuid | Enercon E70-2.3MW | 259.922873 | 590.331564 | 6.960635 | 53.289166 | 85 | 71 | 148 |
| Delfzijl Zuid | Enercon E70-2.3MW | 260.35834 | 590.202484 | 6.96712 | 53.287921 | 85 | 71 | 221 |
| Delfzijl Zuid | Enercon E70-2.3MW | 260.740771 | 590.089216 | 6.972815 | 53.286828 | 85 | 71 | 166 |
| Delfzijl Zuid | Enercon E70-2.3MW | 261.030974 | 590.002864 | 6.977137 | 53.285995 | 85 | 71 | 167 |
| Delfzijl Zuid | Enercon E70-2.3MW | 261.291913 | 589.924931 | 6.981022 | 53.285243 | 85 | 71 | 168 |
| Delfzijl Zuid | Enercon E70-2.3MW | 261.7649 | 589.784887 | 6.988065 | 53.283891 | 85 | 71 | 169 |
| Delfzijl Zuid | Enercon E70-2.3MW | 262.110904 | 589.682933 | 6.993217 | 53.282906 | 85 | 71 | 177 |
| Delfzijl Zuid | Enercon E70-2.3MW | 259.587943 | 589.858106 | 6.955459 | 53.284979 | 85 | 71 | 161 |
| Delfzijl Zuid | Enercon E70-2.3MW | 259.890967 | 589.77026 | 6.959972 | 53.28413 | 85 | 71 | 147 |
| Delfzijl Zuid | Enercon E70-2.3MW | 260.29591 | 589.65205 | 6.966003 | 53.282989 | 85 | 71 | 171 |
| Delfzijl Zuid | Enercon E70-2.3MW | 260.681039 | 589.539455 | 6.971738 | 53.281902 | 85 | 71 | 172 |
| Delfzijl Zuid | Enercon E70-2.3MW | 260.962384 | 589.458786 | 6.975929 | 53.281121 | 85 | 71 | 178 |
| Delfzijl Zuid | Enercon E70-2.3MW | 261.212796 | 589.386475 | 6.979658 | 53.280422 | 85 | 71 | 179 |
| Delfzijl Zuid | Enercon E70-2.3MW | 261.659452 | 589.253521 | 6.986308 | 53.279139 | 85 | 71 | 173 |
| Delfzijl Zuid | Enercon E70-2.3MW | 261.979763 | 589.161173 | 6.991077 | 53.278245 | 85 | 71 | 175 |
| Delfzijl Zuid | Enercon E70-2.3MW | 259.575927 | 589.371548 | 6.95512 | 53.280611 | 85 | 71 | 143 |
| Delfzijl Zuid | Enercon E70-2.3MW | 259.864322 | 589.300094 | 6.959419 | 53.279912 | 85 | 71 | 135 |
| Delfzijl Zuid | Enercon E70-2.3MW | 260.242331 | 589.205417 | 6.965053 | 53.278988 | 85 | 71 | 63 |
| Delfzijl Zuid | Enercon E70-2.3MW | 260.634407 | 589.110325 | 6.970898 | 53.278056 | 85 | 71 | 181 |
| Delfzijl Zuid | Enercon E70-2.3MW | 260.909138 | 589.042112 | 6.974993 | 53.277389 | 85 | 71 | 180 |
| Delfzijl Zuid | Enercon E70-2.3MW | 261.154287 | 588.982437 | 6.978647 | 53.276804 | 85 | 71 | 182 |
| Delfzijl Zuid | Enercon E70-2.3MW | 261.584633 | 588.875902 | 6.985061 | 53.275762 | 85 | 71 | 176 |
| Delfzijl Zuid | Enercon E70-2.3MW | 261.889576 | 588.801081 | 6.989605 | 53.275029 | 85 | 71 | 174 |
| Delfzijl Zuid | Enercon E70-2.3MW | 259.567845 | 589.042121 | 6.954891 | 53.277653 | 85 | 71 | 142 |
| Delfzijl Zuid | Enercon E70-2.3MW | 259.846258 | 588.984811 | 6.959045 | 53.277084 | 85 | 71 | 146 |
| N/A (isolated) | Vestas V47-0.66MW | 242.277221 | 607.409622 | 6.700769 | 53.445755 | 40 | 47 | 95 |
| N/A (isolated) | Vestas V47-0.66MW | 244.559121 | 607.278911 | 6.735066 | 53.444201 | 40 | 47 | 122 |

| | | | | | | | | |
|---|---|---|---|---|---|---|---|---|
| N/A (isolated) | Vestas V47-0.66MW | 243.690061 | 605.26991 | 6.72143 | 53.4263 | 40 | 47 | 102 |
| N/A (isolated) | Vestas V47-0.66MW | 251.917701 | 604.798932 | 6.845023 | 53.420635 | 40 | 47 | 101 |
| N/A (isolated) | Vestas V47-0.66MW | 251.401285 | 603.814238 | 6.836959 | 53.411884 | 40 | 47 | 107 |
| N/A (isolated) | Vestas V47-0.66MW | 253.764943 | 603.85986 | 6.872508 | 53.41186 | 40 | 47 | 7 |
| N/A (isolated) | Vestas V47-0.66MW | 242.595604 | 599.397156 | 6.703353 | 53.373727 | 41 | 47 | 187 |
| N/A (isolated) | Vestas V47-0.66MW | 228.829968 | 603.602173 | 6.497537 | 53.413588 | 40 | 47 | 126 |
| N/A (isolated) | Vestas V47-0.66MW | 228.823949 | 603.264632 | 6.497368 | 53.410556 | 40 | 47 | 209 |
| N/A (isolated) | Vestas V47-0.66MW | 229.192776 | 603.127754 | 6.502882 | 53.409275 | 40 | 47 | 137 |
| N/A (isolated) | Bonus B44-0.6MW | 263.791675 | 590.855744 | 7.018807 | 53.293101 | 42 | 44 | 195 |
| N/A (isolated) | Bonus B44-0.6MW | 264.131662 | 589.740981 | 7.023524 | 53.283018 | 42 | 44 | 44 |
| N/A (isolated) | Bonus B44-0.6MW | 229.338465 | 594.645867 | 6.503094 | 53.333056 | 42 | 44 | 71 |
| N/A (isolated) | Bonus B44-0.6MW | 227.685263 | 596.36537 | 6.478674 | 53.348732 | 42 | 44 | 218 |
| N/A (isolated) | Nordex N43-0.6MW | 258.720015 | 590.177892 | 6.942553 | 53.288021 | 40 | 43 | 48 |
| N/A (isolated) | Nordex N43-0.6MW | 258.733753 | 589.472571 | 6.942531 | 53.281682 | 40 | 43 | 45 |
| N/A (isolated) | Nordex N43-0.6MW | 258.761083 | 588.539969 | 6.942638 | 53.2733 | 40 | 43 | 58 |
| N/A (isolated) | Nordex N43-0.6MW | 259.229215 | 589.408465 | 6.949936 | 53.28101 | 40 | 43 | 69 |
| N/A (isolated) | Nordex N43-0.6MW | 259.234673 | 589.240883 | 6.949963 | 53.279504 | 40 | 43 | 220 |
| N/A (isolated) | EAZ | 250.977 | 591.922 | 6.82699 | 53.30514 | 15 | 12 | 250 |
| N/A (isolated) | EAZ | 250.945 | 591.924 | 6.82653 | 53.30516 | 15 | 12 | 251 |
| N/A (isolated) | EAZ | 250.277 | 591.659 | 6.81642 | 53.3029 | 15 | 12 | 252 |
| N/A (isolated) | EAZ | 229.981 | 596.649 | 6.5132 | 53.35096 | 15 | 12 | 249 |
| N/A (isolated) | EAZ | 258.352 | 592.53 | 6.93779 | 53.30922 | 15 | 12 | 253 |
| N/A (isolated) | 3 blades, unknown type | 238.560594 | 603.465985 | 6.643808 | 53.410926 | 40 | 47 | 202 |
| N/A (isolated) | 3 blades, unknown type | 249.69815 | 602.241034 | 6.810885 | 53.398058 | 42 | 40 | 99 |
| N/A (isolated) | 3 blades, unknown type | 253.532829 | 601.300527 | 6.86675 | 53.388994 | 40 | 48 | 104 |
| N/A (isolated) | 3 blades, unknown type | 236.401778 | 592.624516 | 6.608583 | 53.313867 | 42 | 40 | 208 |
| N/A (isolated) | 3 blades, unknown type | 237.420762 | 594.526957 | 6.62436 | 53.330801 | 40 | 44 | 223 |
| N/A (isolated) | 3 blades, unknown type | 228.259795 | 581.723642 | 6.48395 | 53.217112 | 15 | 7 | 27 |
| N/A (isolated) | 3 blades, unknown type | 254.182107 | 576.563847 | 6.870323 | 53.166587 | 15 | 9 | 150 |
| N/A (isolated) | 3 blades, unknown type | 256.930791 | 588.663139 | 6.91525 | 53.274758 | 42 | 44 | 65 |
| N/A (isolated) | 3 blades, unknown type | 258.207872 | 588.158698 | 6.934225 | 53.269982 | 42 | 49 | 67 |
| N/A (isolated) | 2 blades, unknown type | 261.650974 | 582.811185 | 6.984039 | 53.221272 | 32 | 19 | 121 |
| N/A (isolated) | 2 blades, unknown type | 256.228846 | 579.495627 | 6.90184 | 53.192541 | 32 | 19 | 132 |
| N/A (isolated) | 2 blades, unknown type | 262.265676 | 579.821786 | 6.992242 | 53.194296 | 32 | 19 | 70 |
| N/A (isolated) | 2 blades, unknown type | 263.702426 | 579.427831 | 7.01366 | 53.190468 | 17 | 9 | 62 |
| N/A (isolated) | 2 blades, unknown type | 259.032787 | 576.602244 | 6.942845 | 53.166012 | 15 | 9 | 205 |
| N/A (isolated) | 2 blades, unknown type | 264.665824 | 571.126734 | 7.025184 | 53.115705 | 33 | 17 | 124 |
| N/A (isolated) | 2 blades, unknown type | 242.667978 | 584.032272 | 6.700229 | 53.235687 | 33 | 17 | 133 |
| N/A (isolated) | 2 blades, unknown type | 238.163807 | 594.617055 | 6.635534 | 53.331495 | 32 | 19 | 11 |
| N/A (isolated) | 2 blades, unknown type | 231.119332 | 585.293914 | 6.527598 | 53.248789 | 31 | 14 | 28 |
| N/A (isolated) | 2 blades, unknown type | 226.068758 | 589.225744 | 6.452817 | 53.284808 | 31 | 15 | 214 |
| N/A (isolated) | 2 blades, unknown type | 232.883474 | 594.975816 | 6.556378 | 53.335515 | 32 | 17 | 31 |
| N/A (isolated) | 2 blades, unknown type | 225.631377 | 598.999744 | 6.448421 | 53.372675 | 15 | 9 | 206 |
| N/A (isolated) | 2 blades, unknown type | 226.959712 | 599.974626 | 6.468595 | 53.381255 | 15 | 9 | 134 |
| N/A (isolated) | 2 blades, unknown type | 261.741398 | 588.024744 | 6.987126 | 53.268085 | 32 | 19 | 196 |
| N/A (isolated) | 2 blades, unknown type | 260.986286 | 587.364208 | 6.975594 | 53.262302 | 31 | 20 | 96 |
| N/A (isolated) | 2 blades, unknown type | 235.842207 | 604.763978 | 6.603268 | 53.423006 | 15 | 16 | 226 |